LBNL-40779
UC-413
Preprint

ERNEST ORLANDO LAWRENCE BERKELEY NATIONAL LABORATORY

Transition State Rates and Mass Asymmetric Fission Barriers of Compound Nuclei ^{90,94,98}MO

K.X. Jing, L.G. Moretto, A.C. Veeck,
N. Colonna, I. Lhenry, K. Tso, K. Hanold,
W. Skulski, Q. Sui, and G.J. Wozniak

Nuclear Sciences Division

August 1997

Submitted to
Physical Review C

LOAN COPY
Circulates
For 4 weeks

Bldg. 50 Lib Rm 4014
Lawrence Berkeley National Laboratory

Copy 2

LBNL-40779

DISCLAIMER

This document was prepared as an account of work sponsored by the United States Government. While this document is believed to contain correct information, neither the United States Government nor any agency thereof, nor the Regents of the University of California, nor any of their employees, makes any warranty, express or implied, or assumes any legal responsibility for the accuracy, completeness, or usefulness of any information, apparatus, product, or process disclosed, or represents that its use would not infringe privately owned rights. Reference herein to any specific commercial product, process, or service by its trade name, trademark, manufacturer, or otherwise, does not necessarily constitute or imply its endorsement, recommendation, or favoring by the United States Government or any agency thereof, or the Regents of the University of California. The views and opinions of authors expressed herein do not necessarily state or reflect those of the United States Government or any agency thereof or the Regents of the University of California.

LBNL-40779
UC-413

Transition State Rates and Mass Asymmetric Fission Barriers of Compound Nuclei ^{90,94,98}MO

K. X. Jing, L. G. Moretto, A. C. Veeck[a], N. Colonna[b], I. Lhenry[c], K. Tso[d], K. Hanold[e], W. Skulski[f], Q. Sui[g] and G. J. Wozniak

Nuclear Science Division
Ernest Orlando Lawrence Berkeley National Laboratory
University of California, Berkeley, California 94720 USA

August 27, 1997

This work was supported in part by the Director, Office of Energy Research, Office of High Energy and Nuclear Physics, Division of High Energy Physics, of the U.S. Department of Energy under Contract No. DE-AC03-76SF00098.

Transition State Rates and Mass Asymmetric Fission Barriers of Compound Nuclei ^{90,94,98}Mo

K. X. Jing, L. G. Moretto, A. C. Veeck[a)], N. Colonna[b)], I. Lhenry[c)], K. Tso[d)], K. Hanold[e)], W. Skulski[f)], Q. Sui[g)] and G. J. Wozniak

Nuclear Science Division, Lawrence Berkeley National Laboratory, Berkeley, California 94720

(August 27, 1997)

Abstract

Excitation functions were measured for complex fragments with atomic number Z=5-25 emitted from the compound nuclei ^{90,94,98}Mo produced in the reactions ^{78,82,86}Kr + ^{12}C. Mass-asymmetric fission barriers were extracted by fitting the excitation functions with a transition state formalism. The excitation functions were analyzed to search for atomic number Z and energy E dependent deviations from transition-state-method predictions. No Z and/or E dependent effects that could be attributed to an increased collectivity with increasing mass (charge) of the emitted fragment and associated with transient or stationary solutions of Kramers' diffusion equation are visible. All of the measured excitation functions collapse onto a single universal straight line rigorously consistent with the transition-state predictions. The barriers are compared with the predictions of several macroscopic models. The role of shell effects on the fission barriers is briefly discussed.

I. INTRODUCTION

A. Transition State Rates and Complex Fragment Decay Widths

The transition state method was first introduced into chemistry by Wigner to estimate chemical reaction rates [1], and subsequently applied by Bohr and Wheeler to calculate fission probabilities [2]. In this approach, the fission rate is equated to the flux of phase space density across a suitably located dividing plane normal to the fission coordinate. The suitable location (transition state) is typically chosen at a saddle point in the potential energy surface of a nucleus, which corresponds to a bottleneck in phase space.

The transition-state method has been used successfully, in many subfield of physics and chemistry [3]. The recent literature in nuclear physics, however, provides extensive claims for the failure of the transition state rate to account for measured amounts of pre-scission particle emission (n, p, α or γ) in relatively heavy fissioning systems [4–6]. These claims prompted our attempts to justify the validity of the transition-state method and/or to identify regimes in which deviations might be expected. In a recent paper [7] we have shown that fission excitation functions for 14 compound nuclei covering a mass range from A=186 to 213 can be scaled exactly according to the transition state predictions once the shell effects are accounted for.

In this paper we present experimental excitation functions for many intermediate mass fragments emitted from three different compound nuclei. We extract the associated conditional barriers and compare them with theoretical predictions. We also compare transition state predictions with experimental decay rates for complex fragments, and search for E and Z dependent deviations that may exist.

The transition state expression for the fission decay width is

$$\Gamma_f = \frac{1}{2\pi\rho(E)} \int \rho^*(E - B_f - \varepsilon)\, d\varepsilon \approx \frac{T_f}{2\pi} \frac{\rho^*(E - B_f)}{\rho(E)}, \tag{1}$$

where $\rho(E)$ is the level density of the compound nucleus, $\rho^*(E - B_f - \varepsilon)$ is the level density at the saddle point, B_f is the fission barrier, ε is the kinetic energy over the saddle along

the fission coordinate, and $1/T_f = \partial[\ln \rho^*(x)]/\partial x|_{E-B_f}$.

In the case of fission, the reaction (fission) coordinate can be taken out from both the level densities of the compound nucleus and of the system at the saddle point, and treated explicitly. The fission decay width then takes the form

$$\Gamma_f \approx \hbar\omega \frac{\rho^*(E - B_f)}{\rho^*(E)} \approx \hbar\omega e^{-B_f/T}, \tag{2}$$

where $1/T = \partial[\ln \rho^*(x)]/\partial x|_E$. Now $\rho^*(E)$ and $\rho^*(E - B_f)$ correspond to the same number of degrees of freedom (all but the degree of freedom of the fission coordinate). The quantity $\hbar\omega$ is the oscillator phonon associated with the ground state minimum, and, in general, can be interpreted as the inverse of the channel time constant. In this simplest formulation, one can interpret the fission rate in terms of its two factors: the frequency ω which gives the number of tries per unit time to make it over the fission barrier, and the Boltzmann factor which gives the statistical probability of success per try.

The emission of complex fragments (or mass-asymmetric fission) can be treated in an analogous way by introducing the ridge line of conditional saddle points [8]. Each mass or charge emission can be associated with a conditional saddle (and/or a conditional barrier B_Z) with the constraint of a fixed mass asymmetry (see fig. 1). The locus of all such conditional saddles defines the ridge line in the potential energy surface of a nucleus [8]. The ridge line, which controls the emission of complex fragments, can be measured with techniques similar to those used to determine fission barriers [9,10]. The experimental determination of the precise form of a complete ridge line, however, has only been attempted so far for the light compound nucleus ^{75}Br by Delis *et al* [10].

The emission rate of a fragment of a given mass or charge can still be described by an expression similar to that of Eq. 2. The quantity B_f becomes the conditional barrier B_Z, but what is now the meaning of $\hbar\omega$? Is there a single value of $\hbar\omega$ for all the channels, or does each channel have its own characteristic frequency?

An additional aspect of the problem has been studied by Kramers in his seminal work [11]. Kramers considered the escape of a particle in a potential hole over a barrier through

the shuttling action of Brownian motion, to model the diffusion of the system from the reactant's region to the product's region. The new parameter entering the problem is the viscosity coefficient, which couples the particle's motion to its surrounding medium. The stationary current solution found by Kramers leads to expressions for reaction rates similar to that of the transition-state theory, differing only in the preexponential factor, which now includes the viscosity. More recent work has shown that if the system is forced to start at time $t = 0$ at the ground state minimum, a transient time τ_D exists during which the reaction rate goes from zero to its stationary value [12–18]. Both effects would decrease the overall fission rate compared to the transition state prediction.

These transient effects have been advocated as an explanation for the large number of pre-scission neutrons [4,19–22], charged particles [23–26], and electric dipole γ rays [5,27] observed in the fission of many systems, in apparent contradiction with the predictions of the transition-state method. However, the pre-scission particles can be emitted either before the system reaches the saddle point, or during the descent from saddle to scission. Since only the former component has any bearing on possible deviations of the fission rate from its transition state value, and the separation of the two components is difficult, the experimental evidence is ambiguous. Furthermore, for some systems, the measured scission charged particle multiplicities are consistent with statistical model calculations [28].

Recently, it has been suggested that the viscosity and the transient time may depend on the collectivity of the reaction coordinate [29]. More specifically, the reaction coordinate for a very asymmetric decay (n, p, α emission at the extreme limit) should have little collectivity, while that for a symmetric decay should be very collective. Studies of pre-scission particles as a function of the fragment size claim to have observed such an effect [4,21,29,30]. However, a statistical model, incorporating mass-asymmetry-dependent fission delay times, could not simultaneously reproduce the pre-scission neutron multiplicities and the charge distributions [31].

In this work, we will show that the presence or absence of the effects discussed above may be directly observable in the excitation functions for the emission of fragments with

different Z values. This new technique could be useful to search for systematic deviations from transition state predictions that would indicate the existence of a transient effect.

B. Conditional Barriers and Macroscopic Nuclear Models

The conditional barriers can be evaluated with macroscopic nuclear models, either liquid-drop or liquid-drop-like with certain refinements. Notable among them is the Rotating Finite Range Model (RFRM) [32,33]. It incorporates the finite range nuclear forces acting between the surfaces of an indented shape at the saddle point by using a Yukawa-plus-exponential form of the nuclear potential, which leads to lower saddle-point energies with respect to the rotating liquid-drop model (RLDM) [34]. The RFRM has been quite successful in reproducing fission barriers extracted from excitation functions obtained in heavy-ion reactions ($A > 100$) [35,36]. The RFRM has also been claimed to reproduce the measured conditional barriers for the two previously measured systems ^{75}Br [10] and ^{110,112}In [9].

Boger and Alexander reported recently the conditional barriers for the compound nucleus ^{149}Tb produced by the reaction ^{86}Kr + ^{63}Cu [37]. Their experimental barriers, however, lie between the calculations of the RFRM and the rotating liquid-drop model and show a sizeable disagreement with both. These results may suggest the need for refinements of the RFRM constants to explain the data in the medium mass region.

In a recently developed Thomas-Fermi Model [38,39], an extra binding term for pairs of nucleons, whose wave functions have congruent nodal structures and whose densities have consequently an overlap greater than the average, has been identified. The characteristic features of this "congruence energy" turn out to be: 1) a dependence on the absolute magnitude of the relative neutron excess $(N - Z)/A$, and 2) a doubling of the congruence energy when a nucleus is divided into two non-communicating pieces. Such a process is approximated by the fission of nuclei in the intermediate mass region which proceed through strongly necked-in fission saddle point shapes. Thus, a detailed comparison of the experimentally measured fission barriers in the mass 90 region with Thomas-Fermi model calculations may provide

evidence for this additional binding term.

In this paper we present three nearly complete experimental ridge lines of the conditional barriers for the compound nuclei ^{90,94,98}Mo with neutron to proton ratios N/Z = 1.14, 1.24, and 1.33, respectively. This should provide a test of the predicted N/Z dependence of the conditional barriers by various models. The barriers were obtained by fitting with a transition state formalism [40,41] the measured excitation functions of complex fragments emitted from the compound nuclei formed in the reverse kinematics reactions ^{78,82,86}Kr + ^{12}C. The excitation functions were measured at up to eight different bombarding energies ranging from 6.0 MeV/A to 12.94 MeV/A for each reaction.

The organization of the paper is as the following: The experimental details are given in section II. In section III, the results of the experiment are presented, and the separation of complex fragments of compound nucleus origin from the deep-inelastic component is discussed. The experimental excitation functions and the extracted conditional barriers are presented in section IV. In section V the excitation functions are examined for systematic deviations from the transition state predictions that would indicate the existence of transient effects. Finally, the conclusions of this work are summarized in section VI.

Part of this work has been published previously [42].

II. EXPERIMENT

The experiment was carried out at the 88-Inch Cyclotron of the Lawrence Berkeley Laboratory. Isotopically enriched krypton gas (^{78}Kr, or ^{82}Kr, or ^{86}Kr) was introduced into the Advanced Electron-Cyclotron-Resonance (AECR) source [43] where Kr atoms were ionized to high charge states. After extraction the ionized atoms were injected into the cyclotron, accelerated to the desired energy, and impinged on a target ^{12}C of thickness 1.0 mg/cm^2.

Two position-sensitive ΔE-E quad telescopes were used to detect the fragments emitted in the reactions. Each quad unit consisted of four separate gas-silicon telescopes, and covered 25° in plane and 5° out-of-plane. The active area of each telescope subtended $5^o \times 5^o$ and

the separation between adjacent telescopes was 1.6°. The gas ionization detectors served as ΔE detectors, and were operated at a pressure of 30 torr of isobutane gas. The E-detector in each telescope unit was a 45×45 mm^2 square (5 mm thick) silicon detector with, on the front, strips of low-resistivity material separated by gaps of high-resistivity material to determine and self-calibrate the position [44,45]. Using these telescopes, the energy, the atomic number, the in-plane and out-of-plane angles could be determined for each fragment that traversed the ΔE and stopped in the E-detector. The out-of-plane angle of the incident particle was determined from the ion drift time in the gas ionization detector. The in-plane angle was determined from a resistive division of the energy signal from the silicon detector. These telescopes were designed to measure a continuous angular distribution over 25° lab intervals by overlapping the two quad units so that the dead areas between telescopes were covered. In this way, fairly complete and continuous angular distribution could be obtained in a relatively short amount of beam time.

The atomic charge of the detected particles was determined from the measured ΔE and E-values. An example of ΔE-E spectrum illustrating the range of fragments observed and the Z resolution achieved is shown in fig. 2. Individual fragment Z values up to 15 were resolved. The scattered projectiles and the calibration beams were also used to determine the atomic charge of fragments where one could not resolve individual fragment Z values (Z >15).

The energy calibration of the E and ΔE detectors was performed using the method illustrated in ref [46]. Calibration points were obtained with beams of the same q/A: $^{14}N^{+4}$, $^{28}Si^{+8}$, $^{35}Cl^{+10}$, $^{63}Cu^{+18}$ (10.9 MeV/A) and $^{13}C^{+4}$, $^{26}Mg^{+8}$, $^{39}K^{+12}$, $^{65}Cu^{+20}$, $^{78}Kr^{+24}$ (12.6 MeV/A), impinging directly onto the detectors. The intensity of these beams was attenuated to limit the counting rate to <500 counts/sec. The gas ionization chambers were calibrated at the same time. The energy loss of a calibration beam in the gas section was measured from the difference between the energies deposited in the E detector with and without gas in the ion chamber. Corrections were made for energy losses in the Mylar entrance window of the ionization chamber and in Au absorber used for suppressing electrons and X-rays.

Corrections were also made for the pulse-height defect using the systematics of Moulton *et al* [47]. The energy calibrations were accurate to $\pm 1\%$.

The out-of-plane position was calibrated with a mask, consisting of a matrix of 2 mm holes separated by 4.73 mm, which could be lowered into position remotely. The in-plane position was self-calibrated [44]. The typical position resolution obtained was $\pm 0.2^o$.

To obtain absolute cross sections, the beam charge was collected in a Faraday cup and integrated with a charge-integration module. The charge state of the ^{78,82,86}Kr ions entering the Faraday cup was determined from the systematics of McMahan [48] and/or by means of Rutherford scattering on a ^{197}Au target with a thickness of 40 μg/cm^2. All data, both inclusive and coincidence events, were recorded on magnetic tape and analyzed off-line.

The excitation functions for complex fragment emission from the compound nuclei ^{90,94,98}Mo were measured over a range of excitation energies, from near the barrier to well above, for each compound nucleus. At the lowest energies near the barriers, the cross section for complex fragment emission is quite low. Contaminations from heavier elements in the C target foil can make a substantial contribution to the fragment yield due to the higher excitation energy of the resulting compound nuclei. High purity carbon foils were thus required. In this experiment a C foil prepared by chemical vapor deposition was used [49]. Analysis showed that the contamination level of this carbon foil was $\leq 1.0\%$ (atomic) nitrogen, $\leq 0.8\%$ oxygen, and $\leq 0.10\%$ sodium, substantially purer than foils prepared by the vacuum evaporation method.

For each reaction, the cross section for complex fragment production was determined for up to eight different energies. In order to minimize the time required for beam tuning, a rapid beam change technique [50] was employed. The fast energy change was accomplished by accelerating different charge states at the same main field setting. By keeping the main field constant, the magnet settings for the transport line to the target could be left unchanged. In addition, scaling the injection voltage proportionally to the ion charge also leaves the injection line settings unchanged. Using this technique, the Cyclotron operators were able to change beam energies and ion species in about 30 minutes.

III. RESULTS

A. Velocity Diagram

The reactions were studied in reverse kinematics, namely the heavier ^{78,82,86}Kr nuclei were the projectiles, and the lighter ^{12}C was the target. This technique has two advantages, as illustrated in the kinematics diagram in fig. 3: 1) all the reaction products have a large velocity in laboratory system, and thus are easily identifiable in Z; 2) all the reaction products are forward focused, allowing for a great increase in detection efficiency. In fig. 3 the velocity of the source of the complex fragments is represented by the vector V_S. In the present reactions V_S represents the velocity of the compound nucleus, while V_e represents the velocity of the complex fragment emitted in the center-of-mass from the binary decay of the compound nucleus. V_e has a rather well-defined value, determined mostly by the Coulomb repulsion between the two decay products. The locus of the emission velocities for a particular complex fragment is represented by the circle. V_a and V_b are the velocities of the fragments observed at a given laboratory angle θ. The high (low) velocity solution corresponds to forward (backward) emission in the center-of-mass. In fig. 2 one clearly sees the two ridges associated with the upper and lower kinematic solutions resulting from the binary decay of a fast-moving compound nucleus.

Isotropic emission of complex fragments in the reaction plane is a characteristic feature of the decay of a compound nucleus. To determine if the complex fragments produced in these reactions satisfy this feature, the laboratory energy spectra were transformed into cross-section ($\partial^2\sigma/\partial V_{||}\partial V_{\perp}$) plots in velocity space. The velocity V of each fragment was calculated from its measured charge and kinetic energy. The average mass of a fragment, A, can be determined from its measured atomic number using the empirical formula [51] $A = 2.08Z + 0.0029Z^2$, where Z is the measured atomic number of the fragment. In fig. 4 we present the measured cross section plotted in the $V_{||} - V_{\perp}$ plane for representative complex fragments emitted from 11.21 MeV/A ^{82}Kr+^{12}C reaction. For $Z > 10$ these plots show an

isotropic ring of high cross section (isotropic Coulomb ring). The observed Coulomb rings correspond to the emission of fragments with Coulomb-like velocities from a single source with a well-defined laboratory velocity. These rings have been previously observed [10,51–55] and are indications of binary decays associated with either compound nucleus emission (isotropic) or partially damped deep inelastic processes (anisotropic). The center of each ring defines the laboratory velocity of the source (compound nucleus or composite system) and the radius corresponds to the emission velocity with which the complex fragments are emitted in the source frame. The radius decreases with increasing fragment size (Z-value), as dictated by momentum conservation in the source frame. The distribution of the emission velocities (the width of the ring) results from sequential evaporation of light particles and fluctuations of the Coulomb energy near the scission point arising from thermal fluctuations in various collective degrees of freedom [8]. For the lighter fragments (Z=5-9), the isotropic component is still visible at the forward angles. However, at backward angles, the isotropic component is masked by a partially damped deep inelastic component, which is backward peaked in reverse kinematics for target-like fragments. In fig. 5 representative (Z=8,13,18) Coulomb rings are shown for the reaction ^{82}Kr+^{12}C at four bombarding energies.

The cross section plots in the $V_{\parallel} - V_{\perp}$ plane for the ^{78}Kr+^{12}C and ^{86}Kr+^{12}C reactions are not shown, but they look very similar to those shown above for the ^{82}Kr+^{12}C reaction.

B. Source Velocities and Emission Velocities

The source and emission velocities for each atomic number were obtained from its Coulomb ring by determining the center and average radius. The velocity corresponding to the center of each ring is the experimental source velocity (V_S). Source velocities versus fragment atomic number for the reaction ^{82}Kr+^{12}C are shown in fig. 6 for eight different bombarding energies. The experimental source velocities show very little dependence on the fragment Z-value confirming that all the fragments are emitted by the same source. As expected, these source velocities decrease with decreasing beam energy and agree closely

with the complete fusion velocities V_{cf}, which are indicated in fig. 6 by the horizontal lines.

The statistical error associated with V_S is smaller than the size of the symbols used in fig. 6. The large single error bar shown for each bombarding energy gives an estimate of the systematic error arising from the mass parametrization, the energy calibration of the detectors, and the energy loss in the carbon target. The fact that the data points tend to lie slightly below V_{cf}, which is unphysical, is due to these systematic errors.

The average radii of the Coulomb circles corresponding to the average emission velocities ($< V_e >$) of the fragments for the reaction ^{82}Kr+^{12}C are also shown in fig. 6. The Coulomb nature of these velocities can be inferred both from their magnitude and from their nearly linear dependence upon the atomic number Z of fragments. A calculation of the Coulomb velocities based upon the Viola systematics [56] generalized to asymmetric divisions is shown in the figure by solid lines. In this calculation, the Coulomb energy was taken to be $E_{coul} = 1.44 Z_1 Z_2/[r_0(A_1^{1/3} + A_2^{1/3}) + 2.0]$ where r_0 was determined by equating E_{coul} for symmetric fission (i.e., $Z_1 = Z_2$, $A_1 = A_2$) to the value given by Viola systematics [56]. From conservation of momentum in the center-of-mass, the emission velocities of both fragments in binary decay can be calculated. The agreement between the data and the above crude calculations is generally good, and confirms that the emission velocities are Coulomb-like. At small Z values, the calculated emission velocities are somewhat lower than the experimental data, presumably due to over-estimation, by the above formula, of the distance between two fragments at the scission point for the very asymmetric fission.

Each emission velocity V_e is associated with a distribution having a mean $< V_e >$ and a width $\sigma(V_e)$ as can be seen in the corresponding Coulomb ring. The variance $\sigma(V_e)$ of the distribution for each fragment, which result from the sequential evaporation of light particles and from the thermal fluctuation of the Coulomb energy near the scission point [8], are also plotted in the figure.

Similar source and emission velocities were obtained for the ^{78}Kr+^{12}C and ^{86}Kr+^{12}C reactions, but are not shown.

C. Angular Distributions

Representative angular distributions in the source frame for reactions ^{82}Kr+^{12}C at four different bombarding energies are shown in figs. 7 and 8. The angular distributions for the reactions ^{78}Kr+^{12}C and ^{86}Kr+^{12}C look similar to those for ^{82}Kr+^{12}C, but are not shown. As pointed out in the previous sections, along with the isotropic component, deep-inelastic (target-like or projectile-like) components may also appear in the angular distributions for Z-values near to that of the target or projectile. For intermediate Z-values the isotropic component dominates, and the angular distributions $d\sigma/d\theta_{c.m.}$ are flat over the measured angular range, indicating that these fragments are emitted isotropically in the reaction plane. For fragments with $Z < 10$, the distributions are peaked at backward angles due to the presence of an additional target-like component. The projectile-like component which is expected to peak at forward angles for fragments near the projectile (Z=36), is not observed for $Z \leq 25$.

The isotropic component in the angular distributions is our prime interest. For several other reactions, this same isotropic component has been identified as originating from compound nucleus decay [10,51,52,54,55]. In this work, the source velocity, emission velocity and angular distribution indicate that the isotropic component arises from the decay of the compound nuclei ^{90,94,98}Mo produced in the reactions ^{78,82,86}Kr+^{12}C. The experimental angular distributions $d\sigma/d\theta_{c.m.}$ in the source frame allow one to distinguish and isolate the isotropic from the non-isotropic component.

D. Cross Sections

An isotropic component in the angular distributions can be seen for most fragment Z-values in all three reactions at all bombarding energies. One can separate the isotropic from the anisotropic component and obtain the angle-integrated cross sections. For a flat angular distributions, the angle-integrated cross section for the isotropic component was

determined by extending the average value $d\sigma/d\theta_{c.m.}$ and integrating the extended angular distribution from 0° to 180°. When an angular distribution was not isotropic, a constant equal to the minimum value of $d\sigma/d\theta_{c.m.}$ was taken as the upper limit for the isotropic component, and the cross section was obtained by integrating the constant from 0° to 180°. The non-isotropic components, which we identify with quasi- and deep-inelastic reactions, are concentrated in the general neighborhood of the target and the projectile Z values, and have not been integrated.

The measured charge distributions of the isotropic component for all the bombarding energies are shown in figs. 9, 10 and 11 for ^{94}Mo, ^{90}Mo and ^{98}Mo, respectively, while the corresponding excitation functions are shown in figs. 13, 14 and 15. These cross section data are also tabulated in tables I, II and III. The measured charge distributions of the isotropic component show the left half of the characteristic U-shape associated with the decay of a compound system below the Businaro-Gallone point [57]. The strong increase of the absolute cross sections as well as the evolution in shape of the charge distributions with increasing bombarding energy can be seen in these figures. The observed flattening of the charge distribution with increasing energy can be explained by the increase in the temperature of the system which tends to make all of the decay channels more evenly populated as predicted by the equation $\Gamma_Z \propto exp(-B_Z/T)$.

Odd-even effects are visible in the charge distributions for light fragments where one can clearly resolve fragment Z values. The emission of even Z fragments is prefered over fragments with odd Z values, as shown in the fluctuation patterns of the charge distributions.

E. Coincidence Data

Events in which coincident fragments were detected on opposite sides of the beam axis were analysed. Essentially no coincidences between telescopes on the same side of the beam were observed. This is consistent with the predominantly binary nature of the decays and conservation of momentum. The spectra of the total detected charge $Z_1 + Z_2$ for the reaction

^{82}Kr+^{12}C are shown in fig. 12. The $Z_1 + Z_2$ plots for the reactions ^{78}Kr+^{12}C and ^{86}Kr+^{12}C are similar, and therefore are not shown. Essentially all of the total charge Z_{CN} of the CN is detected in the two fragments, which confirms the binary nature of the reactions. The small difference between Z_{CN} (42) and the detected charge $Z_1 + Z_2$ determines the average number of light charged particles evaporated from the hot fragments. For ^{94}Mo, the average total charge loss at the highest energies is about 2 units, and decreases to about half an unit at the lower energies. For proton rich ^{90}Mo, the charge loss is slightly larger.

For the reactions ^{82}Kr+^{12}C, one sees in the $Z_1 + Z_2$ coincidence spectra an impurity peak at the lowest beam energies (6.16 and 6.90 MeV/A) (see fig. 12.) At these low excitation energies, the cross sections for complex fragment emission from Mo drop dramatically, whereas the cross sections from the heavier impurity compound nuclei drop much more slowly due to their higher excitation energies. Although the contaminant Na, which contributes the most to the contaminate yield, is somewhat heavier than C, the kinetics of both reactions are very similar. One can thus assume the same coincidence efficiency for both reactions. This allows one to correct the measured cross section for the lowest energy by subtracting from it the contributions from the contaminants.

For the reaction ^{86}Kr+^{12}C, a similar impurity peak was observed in the $Z_1 + Z_2$ coincidence spectrum at the lowest bombarding energy (7.71 MeV/A). The contribution from the impurity was subtracted out in the same way.

No impurity peak is apparent for the reaction ^{78}Kr+^{12}C even at the very lowest energy. For this proton-rich system the cross sections for complex fragment emission are much higher than for the more neutron-rich ^{82}Kr+^{12}C and ^{86}Kr+^{12}C systems at the corresponding beam energies (E/A), because of the relatively larger Coulomb energy and hence the lower conditional barriers (see next section). The contribution from the contaminants to this reaction cross section is therefore negligible.

IV. MASS-ASYMMETRIC FISSION BARRIERS

A. Extraction Procedure

In order to extract the mass-asymmetric (conditional) fission barriers, and to examine their sensitivity to a variety of parameters, the experimental excitation functions have been fitted with the function obtained from a transition-state method following the Bohr-Wheeler formalism [2,8,40,41,58] and from Weisskopf theory [59]. In the transition state theory, the reaction coordinate is determined at a suitable point in coordinate space (typically at the saddle point in the case of fission), and the decay rate is equated with the phase space flux across a hyperplane in phase space passing through the saddle point and perpendicular to the fission direction. The decay width for first chance emission of a fragment of charge Z is expressed as

$$\Gamma_Z = \frac{1}{2\pi\rho\left(E - E_r^{gs}\right)} \int_0^{E-B_Z^{eff}} \rho^*\left(E - B_Z^{eff} - \varepsilon\right) d\varepsilon, \tag{3}$$

where $\rho(E - E_r^{gs})$ is the compound nucleus level density; $\rho^*(E - B_Z^{eff} - \varepsilon)$ is the level density at the conditional saddle with kinetic energy ε in the fission mode; and B_Z^{eff} is the effective fission barrier defined as $B_Z^{eff} = B_Z + E_r^s$, with B_Z being the conditional barrier for zero angular momentum. E_r^{gs} and E_r^s are the energy of the rotating ground state relative to the non-rotating macroscopic sphere and the rotational energy of the system at the saddle point, respectively. The neutron and proton decay widths can be written as

$$\Gamma_n = \frac{2mR^2 g'}{\hbar^2 2\pi\rho\left(E - E_r^{gs}\right)} \int_0^{E-B_n^{eff}} \varepsilon\rho\left(E - B_n^{eff} - \varepsilon\right) d\varepsilon, \tag{4}$$

and

$$\Gamma_p = \frac{2mR^2 g'}{\hbar^2 2\pi\rho\left(E - E_r^{gs}\right)} \int_{\varepsilon_C}^{E-B_p^{eff}} \varepsilon\left(1 - \frac{\varepsilon_C}{\varepsilon}\right)\rho\left(E - B_p^{eff} - \varepsilon\right) d\varepsilon, \tag{5}$$

respectively, where: $\rho(E - B_n^{eff} - \varepsilon)$ and $\rho(E - B_p^{eff} - \varepsilon)$ are level densities of the residual nucleus after neutron and proton emission, respectively; ε is the energy of the particle (neutron or proton); m its mass; g' its spin degeneracy ($g' = 2$); R the radius of the nucleus

from which it has been emitted; and ε_C is the Coulomb barrier for proton evaporation which is evaluated in this work with the empirical formula given by Parker *et al* [60]. The effective neutron barrier B_n^{eff} and proton barrier B_p^{eff} are defined as $B_n^{eff} = B_n + E_r^{gs}$ and $B_p^{eff} = B_p + E_r^{gs}$, where B_n is the last neutron binding energy and B_p the last proton binding energy.

As shown in eq. 3, the angular momentum dependence of Γ_Z is taken into account by the addition to the conditional barrier for zero angular momentum B_Z of the rotational energy $E_r^s = \hbar^2\ell(\ell+1)/2\Im_{saddle}$, which is not available for the internal excitation. Here $\Im_{saddle}$ is the moment of inertia about the axis perpendicular to the symmetry axis of the nucleus at the conditional saddle point. The angular momentum ℓ of a compound nucleus is determined by the momentum P of the projectile in the center of mass and the impact parameter b ($\ell\hbar = bP$). Such treatment of the angular momentum is adequate since the calculated moment of inertia of the saddle point is virtually constant over the range of angular momentum considered here.

The formalism presented above requires the use of a specific level-density expression in the widths Γ_n, Γ_p and Γ_Z. It is mainly in these quantities that all of the physical information concerning the nucleus at the saddle point and the residual nucleus after light particle emission is contained. For the level density, we have used the approximate Fermi gas expression $\rho(E) \propto exp[2(aE)^{1/2}]$ where E is the thermal excitation energy of the system and a is the energy level parameter.

The maximum angular momenta $\ell_{\max}$ used in the calculations were not treated as free parameters for each individual fit (for each Z). Instead, they were calculated by the Bass Model [61,62] and adjusted within 1.5 $\hbar$ of the Bass Model predictions to minimize the χ^2 of all the fits simultaneously. Both the $\ell_{\max}$ values used in the fits and the $\ell_{\max}$ values predicted by the Bass Model are listed in table IV.

The angular momentum distribution of the fusion cross section σ_ℓ was parametrized using a Fermi distribution [35,63]

$$\sigma_\ell = \frac{\pi \lambda\!\!\!^{-2} (2\ell + 1)}{1 + exp\left[(\ell - \ell_{\max}) / \delta\ell\right]}, \tag{6}$$

where $\delta\ell$ determines the diffuseness of the distribution and $\ell_{\max}$ is the maximum angular momentum. The value of $\delta\ell$ was chosen to be 1. The fitting was found not to be sensitive to the specific value of $\delta\ell$, since, for $\ell < \ell_{\max}$, variations of $\delta\ell$ from 0 to ∞ result only in changes of σ_ℓ by at most a factor of 2. The expression used in evaluating the cross section for a given fragment is given by:

$$\sigma_Z = \sum_0^{\ell_{\max}} \sigma_\ell P_Z(\ell), \tag{7}$$

where $P_Z(\ell)$ is the probability of emitting a complex fragment. In the expression used for $P_Z(\ell)$, we have included second and third chance emissions. The probability for the first chance emission is Γ_Z/Γ_T where Γ_T is the total decay width taken to be $\Gamma_T = \Gamma_n + \Gamma_p + \Gamma_Z$.

The excitation functions were fitted with two free parameters: the conditional barrier B_Z and the ratio of the level-density parameter at the saddle point to that of the residual nucleus after neutron decay (a_Z/a_n). A level density parameter $a = a_n = A/8$ for the residual nucleus after neutron or proton emission was assumed in the fitting. The fits are excellent for all mass asymmetries and for the entire excitation energy range explored, as shown in figs. 13, 14 and 15 by the solid lines. This consistency of the data with the transition state fits provides strong evidence for the compound nucleus mechanism of the isotropic component in the angular distributions. It also undermines the claims of the existence of transient time effects, which will be discussed in section V in detail. The quality of the fits is also shown in figs. 9, 10 and 11 where charge distributions obtained from the experiment are compared with those obtained from the fits.

B. Role of Shell Effects and the Extraction of the Macroscopic Barriers

The level densities contained in the expressions for Γ_Z, Γ_n and Γ_p should incorporate the corresponding shell effects. In the asymptotic limit of high excitation energy, the shell effects reduce to a constant shift:

$$\begin{aligned} \rho_Z(E - B_Z) &\approx \rho(E - B_Z - \Delta^{sad}_{shell}) \\ \rho_n(E - B_n) &\approx \rho(E - B_n - \Delta^{n-1}_{shell}), \end{aligned} \tag{8}$$

where ρ_Z, ρ_n are the actual level densities; ρ is a smooth functional such as $\rho(E) \propto exp[2(aE)^{1/2}]$; Δ^{sad}_{shell} and Δ^{n-1}_{shell} are the shell effects at the saddle and for the residual nucleus after neutron emission. We have no knowledge about Δ^{sad}_{shell} and, on general grounds, one can perhaps disregard it since shell effects at the saddle are expected to be small. On the other hand, shell effects for residual nuclei can be large, and, in principle at least, should not be disregarded. However, shell effects extracted from ground state masses and liquid drop models notoriously suffer from systematic errors which may be of the order of 1 - 2 MeV. Consequently, if the tabulated shell effects are of the order of 1 - 2 MeV, it may be prudent to disregard them.

What is the effect of such disregard on the extracted barriers?

Let us consider

$$\frac{\Gamma_Z}{\Gamma_T} \approx \frac{\Gamma_Z}{\Gamma_n} \sim \frac{\rho(E - B_Z)}{\rho(E - B_n - \Delta^{n-1}_{shell})} \approx \frac{\rho\left[E - \left(B_Z - \frac{T_Z}{T_n}\Delta^{n-1}_{shell}\right)\right]}{\rho(E - B_n)}, \tag{9}$$

where T_Z and T_n are the temperatures at the saddle and for the residual nucleus, respectively. At high energies where $T_Z/T_n \sim 1$, the extracted barriers would correspond to

$$B_Z^{meas} \approx B_Z^{true} - \Delta^{n-1}_{shell}. \tag{10}$$

In other words, the extracted barrier should be a good approximation to the corresponding macroscopic barrier if $\Delta^{n-1}_{shell} \approx \Delta^{n}_{shell}$, where Δ^{n}_{shell} is the shell effect of the compound nucleus. Since it is necessary for other reasons to measure the emission probabilities down to relatively low energies over the barrier, the extracted barrier should be somewhere between the actual barrier B_Z^{true} and $B_Z^{true} - \Delta^{n-1}_{shell}$. In the cases of ^{90}Mo, ^{94}Mo and ^{98}Mo considered here, the shell effects Δ^{n-1}_{shell} given by Möller *et al.* [64], are -1.21, $+1.07$, -2.46 MeV, respectively. Taking as an example ^{98}Mo which has the largest shell effect, the fit with the shell effects Δ^{n-1}_{shell} included in Γ_n gives "actual" barriers B_Z^{true} that are about 2.0 MeV lower than B_Z^{meas}.

This lowering is to be compared to the shell effects $\Delta^{n-1}_{shell} = -2.46$ MeV. For each isotope, approximately, the same difference would apply for all Z values.

If our excitation functions could be extended to lower energies close enough to the barriers, and to higher energies near or above the plateau of the excitation functions, one might be able to extract the shell effects by using Δ^{n-1}_{shell} as a free parameter in the fit [7].

For the compound nucleus ^{75}Br, which has been studied before [10], the shell effects Δ^{n-1}_{shell} and Δ^{n}_{shell} amount to -4.45 and -4.65 MeV, respectively, as given by ref. [64]. As discussed above, the extracted conditional barriers B_Z for ^{75}Br published in ref. [10] should be interpreted as $B^{true}_Z - \Delta^{n-1}_{shell}$. The corresponding macroscopic barriers should be $B^{macro}_Z = B^{true}_Z - \Delta^{n}_{shell} \approx B_Z + \Delta^{n-1}_{shell} - \Delta^{n}_{shell}$ instead of $B^{macro}_Z = B_Z - \Delta^{n}_{shell}$. For example, the extracted barrier for the symmetric product (Z=17) from fission of ^{75}Br is $B_Z = 37.8$ MeV [10]. The corresponding true barrier B^{true}_Z should be $37.8 + (-4.45) = 33.35$ MeV, and the corresponding macroscopic barrier B^{macro}_Z should therefore be $33.35 - (-4.65) = 38.0$ MeV, not $37.8 - (-4.65) = 42.45$ MeV. A misinterpretation of the published barriers may result in shell corrections made incorrectly when trying to obtain the macroscopic barriers.

C. Extracted Barriers and a_Z/a_n

The extracted conditional barriers B_Z, which correspond approximately to the macroscopic barriers and were designated as B^{meas}_Z in the previous section, and the ratios of level density parameters for the compound nuclei ^{90}Mo, ^{94}Mo, and ^{98}Mo are tabulated in table V and shown in fig. 16.

The barriers increase as a function of fragment Z, peak at symmetry (Z=21) and then fall off. This is the trend expected for the compound nuclei ^{90}Mo, ^{94}Mo, and ^{98}Mo which lie below the Businaro-Gallone point [57]. The slight disagreement between the barriers for complementary Z values near symmetric fission can be understood as due mainly to the poorer identification for the heavier fragment atomic numbers.

The conditional barriers show significant odd-even effects for light fragments, which are

clearly reflected in the charge distributions.

These extracted conditional barriers contain uncertainties from several sources. The most significant one is due to their sensitivity to the level density parameter a_n. This parameter has not been established experimentally for the excitation energy region well above the last neutron binding energy. We chose $a_n = A/8$ which results in excellent fits for all the excitation functions. However, a decrease of the level density parameter a_n from $A/8$ to $A/9$ results in an increase of the extracted value of the barrier by about 1.1 MeV, and in an increase of a_Z/a_n by about 1.2 %, without compromising substantially the quality of the fits. This dependence of the barrier on the level density parameter is encoded in the specific form of level density, i.e., the Fermi gas level density, which we have used in our fitting. It is thus implied that, when making use of the barrier, one should make reference as well to the level density parameter used in extracting the barrier. For comparison, the extracted barriers and a_Z/a_n ratios using three value of a_n (=$A/8$, $A/9$, $A/10$) are listed in table VI for ^{94}Mo.

The energy of the rotating ground state E_r^{gs} was calculated with the RFRM by A. J. Sierk [65]. The rotational energy of the saddle point E_r^s was calculated by assuming a configuration of two nearly-touching spheres separated by 2 fm. If the saddle shapes given by the RFRM [65] are used instead in computing the rotational energy, the extracted barriers shift by -0.24 MeV on average (-0.5 MeV maximum), corresponding to the shift in the rotational energy. In addition, a change of the diffuseness parameter $\delta\ell$ between 0 and 3 ($\delta\ell = 1^{+2}_{-1}\ \hbar$) varies the barriers by $^{+0.35}_{-0.05}$ MeV. The uncertainties from the absolute cross sections carried over through the fitting procedure are listed in table V. Therefore, not including the uncertainty introduced by the variation of level density parameter a_n, we assign an overall uncertainty of 3%, 2%, and 3% for the barriers of ^{90}Mo, ^{94}Mo, and ^{98}Mo, respectively.

D. Comparison with Macroscopic Nuclear Models

The $\ell = 0$ conditional barriers, defined in the macroscopic model calculation as the difference between the mass of the spherical ground state and that of the saddle point shape, are computed for compound nuclei ^{90}Mo, ^{94}Mo, and ^{98}Mo, with the Rotating Finite Range Model and with the Rotating Liquid Drop Model [65]. As discussed previously, the extracted barriers B_Z correspond approximately to $B_Z^{true} - \Delta_{shell}^{n-1}$. The corresponding macroscopic conditional barriers B_Z^{macro} is

$$B_Z^{macro} = B_Z^{true} - \Delta_{shell}^{n} \approx B_Z - (\Delta_{shell}^{n} - \Delta_{shell}^{n-1}), \tag{11}$$

where Δ_{shell}^{n} denotes the shell effect of the compound nucleus under consideration. This equation shows the advantages of the choices made in section IV B. The correction to B_Z is the difference of two shell effects for neighboring nuclei. In this way, the biggest source of systematic errors in the shell effects is eliminated.

In fig. 17, we have plotted the RFRM and the RLDM calculations together with the macroscopic experimental barriers B_Z^{macro} as obtained by eq. 11. Here the values of Δ_{shell}^{n} for ^{90}Mo, ^{94}Mo, and ^{98}Mo were taken to be +0.04, +0.12, and −2.98 MeV, respectively [64], and the corresponding values for $\Delta_{shell}^{n} - \Delta_{shell}^{n-1}$ are therefore +1.25, −0.95, and −0.52 MeV, respectively. One sees that the data fall in between the two model calculations. The shell corrected experimental barriers for ^{90}Mo, ^{94}Mo and ^{94}Mo are 1.7, 4.3, 3.2 MeV higher on average, respectively, than the RFRM predictions. They are also substantially lower than the RLDM predictions, and their difference from the RLDM is even larger than that from the RFRM. These results suggest the need for refinements of both the RFRM constants and the RLDM constants, if not modifications of the models themselves.

Both the RFRM and the RLDM calculations predict the conditional barriers to increase with decreasing N/Z ratio of the compound nuclei. We observed such an isospin dependence in our experimental barriers which are larger for the more neutron rich isotopes. However, the observed isospin dependence is uneven. While the barrier difference between ^{90}Mo and

^{94}Mo is much stronger than predicted, the difference between ^{94}Mo and ^{98}Mo is smaller (see fig. 17).

In both the RFRM and RLDM, the surface energy of a nucleus contains a N-Z surface-symmetry energy term [33] which is a correction to the standard symmetry energy ($\propto (N-Z)^2/A$) in the liquid-drop model. The constant of this surface-symmetry energy term is not well determined, due to the limited range of N-Z asymmetry previously available in the set of measured fission barriers used to determine this parameter. Our measured barriers for three Mo isotopes ranging from the neutron-poor (^{90}Mo) to the neutron-rich (^{98}Mo), with a difference of 8 neutrons, should allow for a better determination of the surface-symmetry energy constant.

E. Congruence Energy and Fission Barriers

The symmetry energy describes the dependence of the binding energy upon $N-Z$. In the liquid-drop model, this symmetry energy takes the form of AI^2, where $I=(N-Z)/A$. Recently, Myers and Swiatecki have identified an extra binding energy term, which is also related to I but takes a different form [38,39]. This extra binding can be described approximately by $C(I) = -10exp(4.2|I|)$ MeV, and can be explained in terms of the granularity of quantal nucleonic density distributions in a potential well. The density distribution of a quantized particle in a potential well consists of cushion-like bumps boxed in by a latticework of the wave function's nodal surfaces. A pair of nucleons with congruent nodal surfaces interacts more strongly (in case of short range forces) than a pair with uncorrelated density modulations. This leads to the pairing effects for a pair of identical particles (n-n or p-p), and to a stronger interaction called the "congruence energy" for a neutron and proton with congruent nodal structures of their wave functions [39]. This "congruence energy" has the interesting property that it is independent of A and thus doubles when a nucleus is divided into two non-communicating pieces. For a nucleus in the intermediate mass region ($A \sim 100$), the saddle shape is very much indented, and the communication between two

nascent fragments is nearly cut off at the saddle point. Consequently, the congruence energy at the saddle should be nearly doubled, and the fission barriers should be consequently reduced.

The doubling of the congruence energy may decrease the fission barriers by as much as 8 MeV for intermediate-mass nuclei, compared to the case in which the congruence energy of the saddle is assumed to be the same as that of the ground state. Fig. 18 shows a comparison of experimental (filled symbols) and calculated (open symbols) fission barriers as a function of the fissility parameter $Z^2/A(1-2.2I^2)$. The curves connect points calculated using the Thomas-Fermi model. The upper curve assumes that the congruence energy is the same at the saddle point as in the ground state, the lower curve that it has doubled. For Radium ($Z^2/A \sim 38$) and heavier nuclei, the experimental fission barriers agree well with the upper curve. For lighter nuclei, however, the data points approach the lower curve. The Radium region is precisely where the saddle-point shapes develop rather suddenly a pronounced neck [66]. As the saddle shape becomes more indented for a lighter fissioning system, the communication between the two pieces is reduced to the extent of being nearly cut-off, giving rise to the doubling of the congruence energy.

The macroscopic symmetric fission barriers for ^{90,94,98}Mo (solid symbols with a fissility $\sim$19) measured in this work and the barrier for ^{75}Br (solid symbol with a fissility near 16.5) measured previously [10] lie close to the lower curve, and lend support to Myers and Swiatecki's argument for the congruence energy. Notice that the barriers for ^{90}Mo, ^{98}Mo and ^{75}Br given here are slightly different from the correspoonding data points in fig. 11 of ref. [38] and in fig. 3 of ref. [39]. This was due to a misinterpretation in refs. [38,39] of our extracted barriers B_Z. The misinterpretation led to the shell corrections which were incorrectly made to our extracted barriers.

V. TRANSITION STATE RATES AND COMPLEX FRAGMENT EXCITATION FUNCTIONS

Now, as discussed in the introduction, we shall search for a Z dependent preexponential factor in the excitation functions for the emission of fragments with different Z values.

Our procedure uses the predictions of the transition-state method as a null hypothesis, and involves only replotting the experimental data without invoking a specific model. The cross section for the emission of a fragment of a given Z value can be written as:

$$\sigma_Z = \sigma_0 \frac{\Gamma_Z}{\Gamma_T} = \sigma_0 \frac{\Gamma_Z}{\Gamma_n + \Gamma_p + \cdots}, \tag{12}$$

where σ_0 is the compound nucleus formation cross section, and Γ_T, Γ_n, Γ_p, Γ_Z are the total-, neutron-, proton-, and Z-decay widths, respectively.

We now rewrite Eq. 12 as follows:

$$\frac{\sigma_Z}{\sigma_0}\Gamma_T \frac{2\pi\rho(E - E_r^{gs})}{T_Z} = \rho^*(E - B_Z - E_r^s), \tag{13}$$

where: T_Z is the temperature at the conditional saddle point; E_r^{gs} is the energy of the rotating ground state; and E_r^s is the saddle point rotational energy. In this way, the left hand side of the equation contains the complex fragment cross section which can be measured, and other calculable quantities that do not depend on Z, except T_Z which is only weakly dependent on it. The right hand side contains only the level density at the conditional saddle calculated at the intrinsic excitation energy over the conditional saddle, which is calculable if the barrier height is known.

By using the standard Fermi gas level density expression, one can rewrite Eq. 13 in the following way which takes out the A-dependence of the level density:

$$\ln\left[\frac{\sigma_Z}{\sigma_0}\Gamma_T \frac{2\pi\rho(E - E_r^{gs})}{T_Z}\right] \Big/ 2\sqrt{a_n} = \frac{\ln R_f}{2\sqrt{a_n}} = \sqrt{\frac{a_Z}{a_n}(E - B_Z - E_r^s)}, \tag{14}$$

where a_Z, a_n are the saddle and ground state level density parameters. A plot of the left hand side of this equation versus the square root of the intrinsic excitation energy over the saddle should give a straight line, and the slope should give the square root of a_Z/a_n.

The excitation functions for a large number of fragment Z values for the systems ^{90}Mo, ^{94}Mo, ^{98}Mo measured in the present work (see figs. 13, 14 and 15), and for systems ^{75}Br, ^{110,112}In measured in our previous works [10,9], allow us to test the above hypothesis. To do so, the E_r^{gs} and E_r^s in eqs. 13 and 14 are taken to be the average values. In the fitting to extract the conditional barriers, the energy of the rotating ground state E_r^{gs} was calculated with the Rotating Finite-Range Model and the rotational energy of the saddle was calculated assuming a configuration of two nearly touching spheres separated by 2 fm. Using the same maximum angular momentum $\ell_{\max}$ as used in the best fit to the excitation functions, one can calculate $<\ell^2>=\ell_{\max}^2/2$ and then the averages of E_r^{gs} and E_r^s accordingly.

Equation 14 suggests that it should be possible to reduce ALL the excitation functions for the emission of different complex fragments from a given system to a single straight line. In fig. 19 all the excitation functions associated with each of four compound nuclei are plotted according to Eq. 14. There are 20, 21, 21, and 20 excitation functions for ^{75}Br, ^{90}Mo, ^{94}Mo, and ^{98}Mo, respectively. We see that all the excitation functions for each Z-value fall with remarkable precision on a single line which is in fact straight, and has a slope near unity. While the straight lines for ^{90}Mo and ^{94}Mo pass closely through zero, the straight line for ^{75}Br shows a small upward shift due to its sizable shell effect (Δ_{shell}^{n-1} =−4.45 MeV [64]). The effect of Δ_{shell}^{n-1} on the scaling is demonstrated as the following. Taking the shell effect into consideration, the Eq. 14 should be rewritten as

$$\ln\left(R_f e^{-\Delta_{shell}^{n-1}/T_n}\right)\Big/2\sqrt{a_n}=\sqrt{\frac{a_Z}{a_n}\left(E-(B_Z+\Delta_{shell}^{n-1})-E_r^s\right)}, \tag{15}$$

that is, approximately, in the explored energy range,

$$\frac{\ln R_f}{2\sqrt{a_n}}=\sqrt{\frac{a_Z}{a_n}\left(E-B_Z-E_r^s\right)}+\frac{1}{2\sqrt{a_n}}\left(-\frac{\Delta_{shell}^{n-1}}{T_Z}+\frac{\Delta_{shell}^{n-1}}{T_n}\right). \tag{16}$$

Since Δ_{shell}^{n-1} is negative and $T_Z < T_n$, an upward shift of the coordinate is resulted. A similar shell effect shift is also discernible for ^{98}Mo.

The sensitivity of the excitation functions to the mass A of the compound nucleus is vividly shown in the fig. 20a, where the logarithm of the reduced mass-asymmetric fission

rate $\ln R_f$ is plotted vs the square root of the intrinsic excitation energy for Z=10 and for five different compound nuclei. The excitation functions are straight lines, but with different slopes for different compound nuclei. After the A dependence is removed, as suggested in Eq. 14, the five lines collapse into a single straight line (see fig. 20b). Similar results are obtained for all the other Z values.

The normalized intercepts of the straight line fits for each Z-value and for all four compound nuclei do not show a statistically significant correlation with Z-value. For example, the linear correlation coefficient determined by Pearson's method is 0.1, where a value close to ± 1 would indicate a linear correlation [67]. This suggests that the quantity $\hbar\omega$ appearing in Eq. 2 does not depend on the Z-value of the emitted fragment.

We can try to collapse ALL the excitation functions for ALL Z values and for all five compound nuclei into a single straight line. The resulting plot for five different compound nuclei is shown in fig. 21. It includes a total of 91 excitation functions, for fragments ranging in Z from 3 to 25. The collapse of all the experimental excitation functions for all the systems onto a single straight line is strong evidence for the validity of the transition state formalism and for the absence of Z- and E-dependent deviations. The present analysis shows that there are no manifest deviations from the transition state formalism in the explored range of excitation energies and charges. In particular, one is led to the following conclusions: 1) Once one removes the phase space associated with the non-reactive degrees of freedom at the conditional saddle point, the reduced rates are IDENTICAL for fragments of all Z-values. Within the experimental sensitivity, the quantity $\hbar\omega$ in Eq. 2 appears to be Z independent. 2) For all fragments, there is no deviation from the expected linear dependence over the excitation energy range from 60-140 MeV. This seems to rule out, for all Z-values, transient time effects which should become noticeable with increasing excitation energy. 3) The slope, which corresponds to the $\sqrt{a_Z/a_n}$, is essentially unity for all Z values of all systems studied. 4) The intercept of the straight line which is associated with the channel frequency ω, is essentially zero and shows no obvious dependence on the fragment Z-values (i.e., the collectivity).

It must be stressed that the observed scaling is an empirical fact. The equation that suggested it (Eq. 13), implies a dominance of first chance emission. While the first chance emission dominates completely at the lower energies, the upper energies explored in this work have not yet reached the generic plateau in excitation functions where the multi-chance emission might be significant (see figs. 13, 14 and 15). For fragments near symmetry for the compound nucleus ^{94}Mo, the first chance emission probability was estimated to be $\geq 40\%$ at the highest energy.

The estimated compound nucleus lifetimes range from $\tau_{CN} \sim 3\times10^{-20}$ sec at the lowest excitation energies to $\tau_{CN} \sim 1\times10^{-21}$ sec at the highest excitation energies. This range is to be compared with transient (delay) times $3\times10^{-20} \leq \tau_D \leq 10^{-19}$ sec that have been inferred from pre-scission particle evaporation [4,68]. These inferred delay times are the sum of the pre-saddle and post-saddle delay times, however. The post-saddle delays have no effect on the fission probabilities. In fig. 22 the effects of a pre-saddle delay time on both the mass asymmetric and the symmetric fission probabilities are estimated for a range of transient times and the calculations are compared with the ^{94}Mo data (Z=13 & Z=21) that cover compound nucleus lifetimes from $\sim 2\times10^{-20}$ to $\sim 2\times10^{-21}$ sec. Assuming a step function for the transient time effects, the fission width can be written as

$$\Gamma_f = \Gamma_f^{(\infty)} \int_0^\infty \lambda(t) e^{-t/\tau_{CN}} d\left(\frac{t}{\tau_{CN}}\right) = \Gamma_f^{(\infty)} e^{-\tau_D/\tau_{CN}}, \tag{17}$$

where $\lambda(t) = 0$ $(t < \tau_D)$ and $\lambda(t) = 1$ $(t \geq \tau_D)$; τ_D is the transient time; $\Gamma_f^{(\infty)}$ denotes the transition state fission width; and τ_{CN} is the compound nucleus life time. In fig. 22 no indication of transient times longer than 1×10^{-20} sec is apparent for either asymmetric or symmetric fission.

VI. SUMMARY

Excitation functions have been measured for complex fragment emission from the compound nuclei ^{90,94,98}Mo produced by the reactions ^{78,82,86}Kr + ^{12}C. Mass asymmetric fission

barriers have been obtained by fitting the excitation functions with a transition state formalism. The observed barriers are several MeV higher on average than the calculation of the Rotating Finite Range Model, and substantially lower than that predicted by the Rotating Liquid Drop Model. An uneven N/Z dependence of the experimental conditional barriers is observed. Odd-even effects are visible for light fragments where one can clearly resolve the fragment Z.

The symmetric fission barriers measured seem to support the hypothesis of a congruence energy term that doubles for the fission of strongly indented saddle-point shapes.

Experimental excitation functions were analyzed to search for atomic number and energy dependent deviations from the transition-state-method predictions. No deviation that can be attributed to transient effects is found in this extended data set. Over ninety excitation functions, for complex fragments from five different nuclei, can be collapsed into a single universal straight line that is nicely consistent with the transition-state predictions.

This work was supported by the Director, Office of the Energy Research, Office of High Energy and Nuclear Physics, Division of Nuclear Physics, of the US Department of Energy under Contract No. DE-AC03-76SF00098.

Present addesses:

[a] McKinsey & Company, Inc, 301 Grant Street, Suite 2600, Pittsburgh, PA15219-1414

[b] INFN, Via Amendola 173, 70126 Bari, Italy

[c] Institut de Physique Nucleaire, Bat 100, 91 406 Orsay cedex, France

[d] CES, Rm 1201, Tai Yau Building, 181 Johnston Road, Wanchai, Hong Kong

[e] Department of Chemistry, University of California at San Diego, La Jolla, CA92093-0314

[f] Nuclear Structrure Research Lab, University of Rochester, Rochester, NY14623

[g] 865 Carlisle Way, Sunnyvale, CA94087

REFERENCES

[1] E. Wigner, Trans. Faraday Soc. **34**, part 1, 29 (1938).

[2] N. Bohr and J. A. Wheeler, Phys. Rev. **56**, 426 (1939).

[3] P. Hänggi, P. Talkner, and M. Borkovec, Rev. Mod. Phys. **62**, 251 (1990).

[4] D. Hilscher and H. Rossner, Ann. Phys. (Paris) **17**, 471-552 (1992), and references therein.

[5] P. Paul and M. Thoennessen, Ann. Rev. Nucl. Part. Sci. **44**, 65 (1994), and references therein.

[6] M. Thoennessen and G. F. Bertsch, Phys. Rev. Lett. **71**, 4303 (1993).

[7] L. G. Moretto, K. X. Jing, R. Gatti, G. J. Wozniak and R. P. Schmitt, Phys. Rev. Lett. **75**, 4186 (1995).

[8] L. G. Moretto, Nucl. Phys. **A247**, 211 (1975).

[9] M. A. McMahan, L. G. Moretto, M. L. Padgett, G. J. Wozniak, L. G. Sobotka and M. G. Mustafa, Phys. Rev. Lett. **54**, 1995 (1985).

[10] D. N. Delis, Y. Blumenfeld, D. R. Bowman, N. Colonna, K. Hanold, K. Jing, M. C. Meng, G. F. Peaslee, G. J. Wozniak and L. G. Moretto, Nucl. Phys. **A534**, 403 (1991).

[11] H. A. Kramers, Physica (Utrecht) **7**, 284 (1940).

[12] P. Grange and H. A. Weidenmüller, Phys. Lett. **96B**, 26 (1980).

[13] P. Grange, J.-Q. Li, and H. A. Weidenmüller, Phys. Rev. **C27**, 2063 (1983).

[14] P. Grange, S. Hassani, H. A. Weidenmüller, A. Gavron, J. R. Nix, and A. J. Sierk, Phys. Rev **C34**, 209 (1986).

[15] H .A. Weidenmüller, J.-S. Zhang, Phys. Rev. **C29**, 879 (1984).

[16] Z.-D. Lu, J.-S. Zhang, R.-F. Feng, and Y.-Z. Zhuo, Z. Phys. **A323**, 477 (1986).

[17] Z.-D. Lu, B. Chen, J.-S. Zhang, and Y.-Z. Zhuo, Phys. Rev. **C42**, 707 (1990).

[18] D. Cha and G. F. Bertsch, Phys. Rev. **C46**, 306 (1992).

[19] A. Gavron, J. R. Beene, B. Cheynis, R. L. Ferguson, F. E. Obenshain, F. Plasil, G. R. Young, G. A. Petitt, M. Jääskeläinen, D. G. Sarantites, and C. F. Maguire, Phys. Rev. Lett. **47**, 1255 (1981); **48**, 835(E) (1982).

[20] E. Holub, D. Hilscher, D. Ingold, U. Jahnke, H. Orf, and H. Rossner, Phys. Rev. **C28**, 252 (1983).

[21] D. J. Hinde, D. Hilscher, H. Rossner, B. Gebauer, M. Lehmann, M. Wilpert, Phys. Rev. **C45**, 1299 (1992).

[22] L. Fiore, G. Viesti, P. F. Bortignon, P. Blasi, G. D'Erasmo, D. Fabris, E. M. Fiore, F. Gramegna, F. Lucarelli, G. Nebbia, A. Pantaleo, V. Paticchio, G. Prete, and J. A. Ruiz, Phys. Rev. **C47**, R1835 (1993).

[23] L. Schad, H. Ho, G.-Y. Fan, B. Lindl, A. Pfoh, R. Wolski, and J. P. Wurm, Z. Phys. **A318**, 179 (1984).

[24] G. F. Peaslee, N. N. Ajitanand, J. M. Alexander, D. Guerreau, R. Lacey, L. C. Vaz, M. Kaplan, M. Kildir, D. J. Moses, D. Logan, and M. S. Zisman, Phys. Rev. **C38**, 1730 (1988).

[25] J. P. Lestone, J. R. Leigh, J. O. Newton, D. J. Hinde, J. X. Wei, J. X. Chen, S. Elfstrom, and D. G. Popescu, Phys. Rev. Lett. **67**, 1078 (1991).

[26] J. P. Lestone, Phys. Rev. Lett. **70**, 2245 (1993).

[27] M. Thoennessen, D. R. Chakrabarty, M. G. Herman, R. Butsch, and P. Paul, Phys. Rev. Lett. **59**, 2860 (1987).

[28] H. Izekoe, N. Shikazono, Y. Nagame, Y. Sugiyama, Y. Tomita, K. Ideno, I. Nishinaka, B. J. Qi, H. J. Kim, A. Iwamoto, and T. Ohtsuki, Phys. Rev. **C46**, 1922 (1992).

[29] D. Hilscher, H. Rossner, B. Cramer, B. Gebauer, U. Jahnke, M. Lehmann, E. Schwinn, M. Wilpert, Th. Wilpert, H. Frobeen, E. Mordhorst, and W. Scobel, Phys. Rev. Lett. **62**, 1099 (1989).

[30] E. Mordhorst, M. Strecker, H. Frobeen, M. Gasthuber, W. Scobel, B. Gebauer, D. Hilscher, M. Lehmann, H. Rossner, and Th. Wilpert, Phys. Rev. **C43**, 716 (1991).

[31] R. J. Charity, Phys. Rev. **C51**, 217 (1995).

[32] A. J. Sierk, Phys. Rev. Lett. **55**, 582 (1985).

[33] A. J. Sierk, Phys. Rev. **C33**, 2039 (1986).

[34] S. Cohen, F. Plasil and W. J. Swiatecki, Ann. of Phys. **82**, 557 (1974).

[35] J. van der Plicht, H. C. Britt, M. M. Fowler, Z. Fraenkel, A. Gavron, J. B. Wilhelmy, F. Plasil, T. C. Awes and G. R. Young, Phys. Rev. **C28**, 2022 (1983).

[36] F. Plasil, T. C. Awes, B. Cheynis, D. Drain, R. L. Ferguson, F. E. Obenshain, A. J. Sierk, S. G. Steadman and G. R. Young, Phys. Rev. **C29**, 1145 (1984).

[37] J. Boger and J. M. Alexander, Phys. Rev. **C50**, 1006 (1994).

[38] W. D. Myers and W. J. Swiatecki, Nucl. Phys. **A601**, 141 (1996).

[39] W. D. Myers and W. J. Swiatecki, Nucl. Phys. **A612**, 249 (1997).

[40] L. G. Moretto, "Fission Probabilities in Lighter Nuclei: A theoretical and experimental investigation of the shell and pairing effects in fissioning nuclei," Physics and Chemistry of Fission 1973, (Vienna: International Atomic Energy Agency, 1974) **I**: 329.

[41] R. Vandenbosch and J. Huizenga, in Nuclear Fission, Chapter 7, (Academic Press,

1973).

[42] L. G. Moretto, K. X. Jing and G. J. Wozniak, Phys. Rev. Lett **74**, 3557 (1995).

[43] Z. Q. Xie, C. M. Lyneis, R. S. Lam and S. A. Lundgren, Rev. Sci. Instrum. **62**, 775 (1991).

[44] W. L. Kehoe, A. C. Mignerey, A. Moroni, I. Iori, G. F. Peaslee, N. Colonna, K. Hanold, D. R. Bowman, L. G. Moretto, M. A. McMahan, J. T. Walton and G. J. Wozniak, Nucl. Instr. and Meth. **A311**, 258 (1992).

[45] J. T. Walton, H. A. Sommer, G. J. Wozniak, G. F. Peaslee, D. R. Bowman, W. L. Kehoe and A. Moroni, IEEE Trans. Nucl. Sci. **37**, 1578 (1990).

[46] M. A. McMahan, G. J. Wozniak, C. M. Lyneis, D. R. Bowman, R. J. Charity, Z. H. Liu, L. G. Moretto, W. L. Kehoe, A. C. Mignerey and M. N. Namboodiri, Nucl. Instr. and Meth. **A253**, 1 (1986).

[47] J. B. Moulton, J. E. Stephenson, R. P. Schmitt and G. J. Wozniak, Nucl. Instr. and Meth. **157**, 325 (1978).

[48] M. A. McMahan, R. F. Lebed and B. Feinberg, The 1989 IEEE Particle Accelerator Conference, Chicago, Ill., March 1989.

[49] A. C. Veeck, K. X. Jing, Q. Sui, L. G. Moretto and G. J. Wozniak, Nucl. Instr. and Meth. **B108**, 159 (1996).

[50] D. J. Clark and G. J. Wozniak, Nucl. Instr. and Meth. **A295**, 34 (1990).

[51] R. J. Charity, D. R. Bowman, Z. H. Liu, R. J. McDonald, M. A. McMahan, G. J. Wozniak, L. G. Moretto, S. Bradley, W. L. Kehoe and A. C. Mignerey, Nucl. Phys. **A476**, 516 (1988).

[52] R. J. Charity, M. A. McMahan, G. J. Wozniak, R. J. McDonald, L. G. Moretto, D. G. Sarantites, L. G. Sobotka, G. Guarino, A. Pataleo, L. Fiore, A. Gobbi and K. D.

Hildenbrand, Nucl. Phys. **A483**, 371 (1988).

[53] R. J. Charity, M. A. McMahan, D. R. Bowman, Z. H. Liu, R. J. McDonald, G. J. Wozniak, L. G. Moretto, S. Bradley, W. L. Kehoe, A. C. Mignerey and M. N. Namboodiri, Phys. Rev. Lett. **56**, 1354 (1986).

[54] R. J. Charity, K. X. Jing, D. R. Bowman, M. A. McMahan, G. J. Wozniak, L. G. Moretto, N. Colonna, G. Guarino, A. Pantaleo, L. Fiore, A. Gobbi and K. D. Hildenbrand, Nucl. Phys. **A511**, 59 (1990).

[55] H. Y. Han, K. X. Jing, E. Plagnol, D. R. Bowman, R. J. Charity, L. Vinet, G. J. Wozniak and L. G. Moretto, Nucl. Phys. **A492**, 138 (1989).

[56] V. E. Viola, K. Kwiatkowski and M. Walker, Phys. Rev. **C31**, 1550 (1985).

[57] U. L. Businaro and S. Gallone, Nuovo Cimento **1**, 629 (1955); **1**, 1277 (1955).

[58] L. G. Moretto and G. J. Wozniak, Prog. Part. & Nucl. Phys. **21**, 401 (1988).

[59] V. F. Weisskopf and P. H. Ewing, Phys. Rev. **57**, 472 (1940).

[60] W. E. Parker, M. Kaplan, D. J. Moses, G. La Rana, D. Logan, R. Lacey, J. M. Alexander, D. M. de Castro Rizzo, P. DeYoung, R. J. Welberry and J. T. Boger, Phys. Rev. **C44**, 774 (1991).

[61] R. Bass, Nucl. Phys. **A231**, 45 (1974).

[62] R. Bass, Phys. Rev. Lett. **39**, 265 (1977).

[63] B. Haas, G. Duchene, F. A. Beck, T. Byrski, C. Gehringer, J. C. Merdinger, A. Nourredine, V. Rauch, J. P. Vivien, J. Barrette, S. Tobbeche, E. Bozek, J. Styczen, J. Keinonen, J. Dudek and W. Nazarewicz, Phys. Rev. Lett. **54**, 398 (1985).

[64] P. Möller, J. R. Nix, W. D. Myers and W. J. Swiatecki, Los Alamos National Laboratory, LA-UR-3083 (1994).

[65] A. J. Sierk, Private communication.

[66] S. Cohen and W. J. Swiatecki, Ann. of Phys. **22**, 406 (1963).

[67] W. H. Press, S. A. Teukolsky, W. T. Vetterling and B. P. Flannery, *Numerical Recipes in FORTRAN: The Art of Scientific Computing* (Cambridge University Press, Cambridge, 1992), 2nd ed.

[68] J. O. Newton, Pramãna - J. Phys. **33**, 175 (1989), and references therein.

TABLES

TABLE I. The total cross section of the isotropic component in the angular distributions (see figs. 7 and 8) as a function of both the fragment Z-value and the excitation energy E of the compound nucleus ^{94}Mo formed in the ^{82}Kr+^{12}C reaction at eight bombarding energies (E_{beam}). The uncertainties from the normalization of the cross sections are included in the error bars.

TABLE II. Same as in table I for the compound nucleus ^{90}Mo formed in the ^{78}Kr+^{12}C reaction.

TABLE III. Same as in table I for the compound nucleus ^{98}Mo formed in the ^{86}Kr+^{12}C reaction.

TABLE IV. The maximum angular momentum ℓ_{max} for fusion. In the column ℓ_{max} (Bass) are the values predicted by the Bass Model [61,62]. In the column ℓ_{max} (fits) are the values used in the fits.

TABLE V. The mass-asymmetric fission barriers (B_Z) and the ratio of the level density parameters (a_Z/a_n) for compound nuclei ^{90}Mo, ^{94}Mo, and ^{98}Mo, extracted from the fitting of the excitation functions with a transition state formalism. B_Z should be interpreted as $B_Z \approx B_Z^{true} - \Delta_{shell}^{n-1}$ (see text). The uncertainties given are the standard errors arising solely from the uncertainties of the cross sections. The parameters used in the fitting are: $a_n = A/8$, $\delta\ell = 1\ \hbar$. The uncertainties arising from these parameters are discussed in the text and are not included in the table.

TABLE VI. The extracted barriers B_Z and a_Z/a_n values for ^{94}Mo with three different values of the level density parameter a_n (=$A/8$, $A/9$, $A/10$). Other parameters are kept the same as in the table V.

FIGURES

FIG. 1. Schematic potential-energy surface as a function of the reaction and mass-asymmetry coordinates for a light nucleus.

FIG. 2. Density plot of ΔE versus E for the reaction 11.21 MeV/A ^{82}Kr + ^{12}C for fragments detected at forward laboratory angles.

FIG. 3. Schematic representation of the binary decay by fragment emission of a compound nucleus produced in a reverse kinematics reaction (see text).

FIG. 4. Contours of the experimental cross section $\partial^2\sigma/\partial V_\perp \partial V_{||}$ in the $V_\perp - V_{||}$ plane for representative Z-values detected in the reaction 11.21 MeV/A ^{82}Kr+^{12}C. The magnitudes of the contour levels are in linear scale. The dashed lines represent the limits of the geometrical coverage of the experimental devices. The dotted lines show the energy thresholds of the detectors. The arrow on the vertical axis denotes the complete fusion velocity.

FIG. 5. Same as in fig. 4 for Z=8, 13, 18 at four bombarding energies.

FIG. 6. In the upper part of each octant are shown the source velocities V_S ($\times$) extracted from the invariant cross-section plots (see figs. 4 and 5) for each Z-species produced in the 12.19, 11.21, 10.27, 9.37, 8.51, 7.69, 6.90 and 6.16 MeV/A ^{82}Kr+^{12}C reactions. The single large error bar for each data set indicates the possible systematic error due to the mass parameterization, energy calibration, and energy losses in the target and in the detector entrance window. The complete fusion velocity is indicated by the horizontal line. In the lower portion of each octant are shown the average emission velocities $< V_e >$ ($\diamond$) that correspond to the mean radii of the Comlomb circles exemplified in figs. 4 and 5. For comparison, a calculation based on the Viola systematics [56] (solid line) is also shown. The variances $\sigma(V_e)$ of the velocity distributions in the source frame are shown by the open squares ($\square$).

FIG. 7. Angular distributions $d\sigma/d\theta_{c.m.}$ in the source frame for representative Z-values produced in the 12.19 and 11.21 MeV/A ^{82}Kr+^{12}C reactions. The numbers to the right indicate the factor by which each set of experimental points was multiplied, in order to separate it from its neighboring set of points for visual display purpose.

FIG. 8. Same as in fig. 7 for the 10.27 and 8.51 MeV/A ^{82}Kr+^{12}C reactions.

FIG. 9. Charge distributions of the isotropic component in the angular distributions (see figs. 7 and 8) for the ^{82}Kr+^{12}C reaction at eight bombarding energies. The uncertainties from the normalization of cross sections are not included in the error bars for clarity. The solid lines represent the best fit to the experimental data (see text and fig. 13). The values for $\ell_{\max}$ shown are the maximum angular momenta used in the fitting, which were calculated with the Bass Model [61,62] and adjusted slightly within 1.5 $\hbar$ of the Bass Model predictions (see also the table IV) to minimize the χ^2 of the fits.

FIG. 10. Same as in fig. 9 for the ^{78}Kr+^{12}C reaction at five bombarding energies.

FIG. 11. Same as in fig. 9 for the ^{86}Kr+^{12}C reaction at seven bombarding energies.

FIG. 12. The relative yield of coincidence events versus the sum of the atomic numbers of the two fragments detected in coincidence for the ^{82}Kr+^{12}C reaction at eight different bombarding energies. The arrows indicate the total charge (42) of the projectile and the target. The numbers to the left of the arrows are the mean total detected charge at the corresponding bombarding energies. An impurity peak at larger charge can be identified at the bombarding energy 6.90 MeV/A, which becomes more pronounced at the lowest bombarding energy 6.16 MeV/A.

FIG. 13. The excitation functions for emission of complex fragments from the compound nucleus ^{94}Mo produced in ^{82}Kr+^{12}C reaction. The abscissa is the excitation energy of the compound nucleus. The curves are fits with the parameters shown in fig. 16 and table V. The number to the right indicates the factor by which each curve and the set of experimental points was multiplied, in order to separate it from its neighboring curves and data sets for visual display purpose.

FIG. 14. Same as in fig. 13 for the compound nucleus ^{90}Mo produced in ^{78}Kr+^{12}C reaction.

FIG. 15. Same as in fig. 13 for the compound nucleus ^{98}Mo produced in ^{86}Kr+^{12}C reaction.

FIG. 16. The mass-asymmetric fission barriers (B_Z) and the ratio of the level density parameters (a_Z/a_n) for compound nuclei ^{90}Mo, ^{94}Mo, and ^{98}Mo, extracted from the fitting of the excitation functions. The error bars shown are the standard errors arising solely from the uncertainties of the cross sections. The parameters used in the fitting: $a_n = A/8$, $\delta\ell = 1\ \hbar$. The uncertainties arising from choice of these parameters are not included in the error bars. B_Z should be interpreted as $B_Z^{true} - \Delta_{shell}^{n-1}$. See text.

FIG. 17. The comparison of the shell corrected experimental barriers $B_Z^{macro} = B_Z - (\Delta_{shell}^{n} - \Delta_{shell}^{n-1})$ with the Rotating Finite Range Model (RFRM) and the Rotating Liquid Drop Model (RLDM) calculations for ^{90,94,98}Mo. See also the text.

FIG. 18. Calculated fission barriers (open symbols) and measurements (solid symbols) corrected for ground-state shell effects. The open diamonds assume that the congruence energy at the saddle point is the same as in the ground state, the open squares assume that it has doubled. "Fissility" is defined as $Z^2/A(1 - 2.2I^2)$ where $I = (N - Z)/A$. The four experimental data points in the fissility range 15-20 correspond to the macroscopic conditional barriers for the symmetric products from fission of the compound nuclei ^{75}Br [10], ^{90}Mo, ^{94}Mo and ^{98}Mo. [The other data points and the curves are from W. D. Myers and W. J. Swiatecki, ref. [39]].

FIG. 19. The logarithm of the reduced mass-asymmetric fission rate R_f as defined in eq. 14 divided by $2a_n{}^{1/2}$ versus the square root of the intrinsic excitation energy for four compound nuclei: ^{75}Br (a), ^{90}Mo (b), ^{94}Mo (c) and ^{98}Mo (d). The solid lines are the linear fits to the data. The error bars are smaller than the size of symbols.

FIG. 20. (a) The quantities ln R_f and (b) ln R_f divided by $2a_n{}^{1/2}$ vs the square root of the intrinsic excitation energy for Z=10 fragments emitted from the compound nuclei: ^{75}Br, ^{90}Mo, ^{94}Mo, ^{98}Mo and ^{110,112}In. The A dependence of R_f via a_n is shown in (a), while this A dependence is removed in (b). See fig. 19.

FIG. 21. The same as fig. 19 with the data for all the four compound nuclei and ^{110,112}In shown in a single plot. The straight line is the linear fit to all the data points. See fig. 19.

FIG. 22. The same as fig. 19 with the data only for fragment Z=13 (a) and fragment Z=21 (b) emitted from the compound nucleus ^{94}Mo. The compound nucleus lifetime τ_{CN} (sec) is indicated on the top. In each case (a or b): the straight line is a linear fit to the data points; the three additional lines marked α, β, and γ represent calculations (see text) assuming that no fission occurs during the transient times of 1×10^{-20}, 2×10^{-20}, and 5×10^{-20} sec, respectively.

E_{beam} (MeV/A)	12.19	11.21	10.27	9.37	8.51	7.69	6.90	6.16
E (MeV)	135.4	125.2	115.3	105.9	96.9	88.3	80.1	72.3
Z	σ_Z (mb)							
5	4.55±0.91	3.14±0.63	1.78±0.36	1.16±0.23	0.56±0.11	0.28±0.07	$(8.9\pm2.7)10^{-2}$	$(2.1\pm0.8)10^{-2}$
6	6.82±2.05	5.38±1.61	3.44±1.03	2.28±0.68	1.21±0.36	0.60±0.21	0.22±0.09	$(4.4\pm2.2)10^{-2}$
7	2.56±0.51	1.79±0.36	1.09±0.22	0.64±0.13	0.31±0.06	0.11±0.03	$(3.0\pm0.9)10^{-2}$	$(5.0\pm2.0)10^{-3}$
8	2.70±0.54	1.57±0.31	1.02±0.20	0.56±0.11	0.26±0.05	0.10±0.03	$(2.6\pm0.8)10^{-2}$	$(3.3\pm1.3)10^{-3}$
9	1.05±0.26	0.76±0.19	0.42±0.11	0.21±0.05	$(6.4\pm1.6)10^{-2}$	$(2.4\pm0.7)10^{-2}$	$(4.6\pm1.6)10^{-3}$	$(4.4\pm2.2)10^{-4}$
10	1.31±0.26	0.84±0.17	0.50±0.10	0.24±0.05	0.11±0.02	$(3.0\pm0.7)10^{-2}$	$(4.8\pm1.4)10^{-3}$	$(5.7\pm2.3)10^{-4}$
11	1.09±0.29	0.70±0.21	0.38±0.11	0.17±0.05	$(6.7\pm2.0)10^{-2}$	$(2.1\pm0.7)10^{-2}$	$(2.8\pm1.1)10^{-3}$	$(2.6\pm1.3)10^{-4}$
12	1.15±0.25	0.73±0.14	0.40±0.07	0.17±0.03	$(7.0\pm1.6)10^{-2}$	$(2.0\pm0.5)10^{-2}$	$(3.1\pm1.1)10^{-3}$	$(3.6\pm1.6)10^{-4}$
13	1.00±0.22	0.57±0.11	0.30±0.06	0.13±0.03	$(4.7\pm1.1)10^{-2}$	$(1.2\pm0.3)10^{-2}$	$(1.7\pm0.5)10^{-3}$	$(2.2\pm1.0)10^{-4}$
14	0.87±0.19	0.58±0.11	0.29±0.05	0.12±0.02	$(4.6\pm1.1)10^{-2}$	$(1.1\pm0.3)10^{-2}$	$(1.7\pm0.5)10^{-3}$	$(2.8\pm1.2)10^{-4}$
15	0.64±0.14	0.46±0.09	0.24±0.05	$(9.0\pm1.9)10^{-2}$	$(3.3\pm0.8)10^{-2}$	$(8.1\pm2.1)10^{-3}$	$(9.9\pm3.3)10^{-4}$	$(1.6\pm0.8)10^{-4}$
16	0.69±0.19	0.41±0.10	0.21±0.05	$(8.3\pm2.1)10^{-2}$	$(3.0\pm0.9)10^{-2}$	$(6.8\pm2.2)10^{-3}$	$(8.6\pm3.3)10^{-4}$	$(1.8\pm1.0)10^{-4}$
17	0.55±0.15	0.36±0.09	0.19±0.05	$(7.0\pm1.8)10^{-2}$	$(2.2\pm0.7)10^{-2}$	$(4.8\pm1.7)10^{-3}$	$(6.4\pm2.8)10^{-4}$	$(8.9\pm5.4)10^{-5}$
18	0.61±0.17	0.35±0.09	0.16±0.04	$(6.5\pm1.7)10^{-2}$	$(2.3\pm0.7)10^{-2}$	$(3.8\pm1.3)10^{-3}$	$(7.0\pm3.1)10^{-4}$	$(1.1\pm0.7)10^{-4}$
19	0.60±0.17	0.35±0.09	0.15±0.04	$(6.1\pm1.6)10^{-2}$	$(2.0\pm0.7)10^{-2}$	$(3.5\pm1.2)10^{-3}$	$(5.5\pm2.5)10^{-4}$	$(1.0\pm0.6)10^{-4}$
20	0.61±0.17	0.37±0.09	0.16±0.04	$(5.8\pm1.6)10^{-2}$	$(1.9\pm0.6)10^{-2}$	$(3.5\pm1.3)10^{-3}$	$(4.9\pm2.5)10^{-4}$	$(1.1\pm0.7)10^{-4}$
21	0.65±0.18	0.39±0.09	0.16±0.04	$(6.0\pm1.7)10^{-2}$	$(1.7\pm0.6)10^{-2}$	$(2.9\pm1.1)10^{-3}$	$(5.3\pm2.7)10^{-4}$	$(1.0\pm0.6)10^{-4}$
22	0.65±0.18	0.41±0.10	0.17±0.04	$(6.5\pm1.8)10^{-2}$	$(1.9\pm0.7)10^{-2}$	$(2.7\pm1.0)10^{-3}$	$(5.2\pm2.6)10^{-4}$	
23	0.57±0.16	0.36±0.09	0.16±0.04	$(6.9\pm1.9)10^{-2}$	$(1.8\pm0.7)10^{-2}$	$(3.1\pm1.2)10^{-3}$	$(4.5\pm2.5)10^{-4}$	
24	0.49±0.14	0.34±0.08	0.17±0.04	$(7.9\pm2.2)10^{-2}$	$(1.9\pm0.8)10^{-2}$	$(3.2\pm1.3)10^{-3}$	$(6.1\pm3.4)10^{-4}$	
25	0.49±0.14	0.34±0.09	0.17±0.04	$(7.3\pm2.0)10^{-2}$	$(1.9\pm0.7)10^{-2}$	$(4.3\pm1.7)10^{-3}$	$(7.1\pm3.9)10^{-4}$	

E_{beam} (MeV/A)	11.37	10.38	8.52	7.64	6.03
E (MeV)	124.3	114.0	94.6	85.5	68.7
Z			σ_Z (mb)		
5	3.78±0.76	2.60±0.52	0.85±0.17	0.35±0.08	$(4.5\pm1.8)10^{-2}$
6	9.65±2.90	7.03±2.11	2.59±0.78	1.40±0.49	0.20±0.10
7	3.32±0.66	2.14±0.43	0.62±0.12	0.24±0.06	$(2.1\pm0.8)10^{-2}$
8	3.55±0.71	2.38±0.48	0.74±0.15	0.32±0.08	$(2.7\pm1.1)10^{-2}$
9	1.32±0.26	0.83±0.17	0.22±0.04	$(7.0\pm1.8)10^{-2}$	$(3.0\pm1.2)10^{-3}$
10	1.96±0.39	1.24±0.25	0.30±0.06	$(9.9\pm2.5)10^{-2}$	$(3.5\pm1.4)10^{-3}$
11	1.75±0.35	0.93±0.19	0.24±0.05	$(7.6\pm1.9)10^{-2}$	$(2.7\pm1.1)10^{-3}$
12	2.01±0.41	1.28±0.25	0.30±0.06	0.10±0.03	$(3.3\pm1.4)10^{-3}$
13	1.63±0.34	1.00±0.19	0.21±0.05	$(6.4\pm1.6)10^{-2}$	$(2.1\pm0.8)10^{-3}$
14	1.79±0.37	1.10±0.21	0.25±0.05	$(8.0\pm1.9)10^{-2}$	$(2.3\pm0.9)10^{-3}$
15	1.30±0.27	0.79±0.15	0.15±0.03	$(5.0\pm1.2)10^{-2}$	$(1.4\pm0.6)10^{-3}$
16	1.23±0.32	0.77±0.19	0.15±0.04	$(4.5\pm1.3)10^{-2}$	$(1.2\pm0.5)10^{-3}$
17	1.02±0.27	0.58±0.14	0.12±0.04	$(2.7\pm0.8)10^{-2}$	$(6.5\pm3.4)10^{-4}$
18	1.05±0.28	0.58±0.14	$(9.2\pm2.9)10^{-2}$	$(2.3\pm0.8)10^{-2}$	$(5.0\pm2.7)10^{-4}$
19	1.15±0.30	0.56±0.14	$(9.0\pm2.8)10^{-2}$	$(1.8\pm0.6)10^{-2}$	$(3.8\pm2.3)10^{-4}$
20	1.20±0.31	0.59±0.15	0.11±0.03	$(2.1\pm0.7)10^{-2}$	$(5.0\pm3.0)10^{-4}$
21	1.12±0.29	0.64±0.16	$(9.2\pm2.8)10^{-2}$	$(2.4\pm0.8)10^{-2}$	$(5.5\pm3.2)10^{-4}$
22	1.23±0.33	0.66±0.16	$(9.2\pm3.0)10^{-2}$	$(2.3\pm0.8)10^{-2}$	$(6.7\pm4.0)10^{-4}$
23	1.17±0.31	0.66±0.16	0.10±0.04	$(2.8\pm1.0)10^{-2}$	$(6.5\pm3.7)10^{-4}$
24	1.07±0.29	0.69±0.17	0.12±0.04	$(2.7\pm1.0)10^{-2}$	$(6.5\pm3.7)10^{-4}$
25	1.07±0.29	0.67±0.17	0.16±0.06	$(4.0\pm1.7)10^{-2}$	$(1.1\pm0.6)10^{-3}$

E_{beam} (MeV/A)	12.94	11.98	11.06	10.17	9.31	8.49	7.71
E (MeV)	141.1	131.0	121.3	111.9	102.9	94.3	86.0
Z	σ_Z (mb)						
5	3.47±1.04	3.05±0.91	1.66±0.50	1.02±0.31	0.51±0.18	0.27±0.09	0.11±0.04
6	4.46±1.34	2.74±0.82	1.93±0.58	1.31±0.39	0.67±0.24	0.40±0.14	0.16±0.07
7	1.93±0.58	1.23±0.37	0.60±0.18	0.39±0.12	0.17±0.06	$(8.7\pm3.1)10^{-2}$	$(2.9\pm1.1)10^{-2}$
8	1.26±0.38	0.89±0.27	0.44±0.13	0.26±0.08	0.12±0.04	$(6.5\pm2.3)10^{-2}$	$(1.9\pm0.8)10^{-2}$
9	0.72±0.22	0.42±0.13	0.22±0.07	0.11±0.03	$(4.8\pm1.7)10^{-2}$	$(2.7\pm0.9)10^{-2}$	$(6.0\pm2.4)10^{-3}$
10	0.91±0.27	0.68±0.21	0.48±0.14	0.22±0.07	$(9.1\pm3.2)10^{-2}$	$(2.1\pm0.7)10^{-2}$	$(4.3\pm1.9)10^{-3}$
11	0.64±0.13	0.39±0.12	0.21±0.06	0.12±0.04	$(4.8\pm1.7)10^{-2}$	$(1.1\pm0.4)10^{-2}$	$(2.6\pm1.2)10^{-3}$
12	0.49±0.10	0.29±0.09	0.18±0.05	$(8.8\pm2.7)10^{-2}$	$(3.3\pm1.2)10^{-2}$	$(1.1\pm0.4)10^{-2}$	$(1.6\pm0.6)10^{-3}$
13	0.37±0.07	0.27±0.08	0.16±0.05	$(6.4\pm1.9)10^{-2}$	$(2.4\pm0.9)10^{-2}$	$(7.5\pm2.6)10^{-3}$	$(1.5\pm0.6)10^{-3}$
14	0.33±0.07	0.21±0.04	$(9.9\pm2.0)10^{-2}$	$(5.2\pm1.0)10^{-2}$	$(2.0\pm0.5)10^{-2}$	$(6.7\pm2.0)10^{-3}$	$(1.2\pm0.4)10^{-3}$
15	0.24±0.05	0.14±0.03	$(7.0\pm1.4)10^{-2}$	$(4.1\pm0.8)10^{-2}$	$(1.6\pm0.4)10^{-2}$	$(4.2\pm1.3)10^{-3}$	$(1.1\pm0.4)10^{-3}$
16	0.22±0.04	0.14±0.03	$(6.7\pm1.3)10^{-2}$	$(3.6\pm0.7)10^{-2}$	$(1.5\pm0.4)10^{-2}$	$(4.5\pm1.3)10^{-3}$	$(8.4\pm3.0)10^{-4}$
17	0.22±0.04	0.12±0.02	$(6.2\pm1.2)10^{-2}$	$(3.2\pm0.6)10^{-2}$	$(1.3\pm0.3)10^{-2}$	$(3.0\pm0.9)10^{-3}$	$(7.1\pm2.5)10^{-4}$
18	0.20±0.04	0.12±0.02	$(5.8\pm1.2)10^{-2}$	$(3.0\pm0.6)10^{-2}$	$(1.1\pm0.3)10^{-2}$	$(2.9\pm0.9)10^{-3}$	$(5.5\pm1.9)10^{-4}$
19	0.21±0.04	0.11±0.02	$(5.3\pm1.1)10^{-2}$	$(3.0\pm0.6)10^{-2}$	$(1.1\pm0.3)10^{-2}$	$(2.8\pm0.8)10^{-3}$	$(7.3\pm2.6)10^{-4}$
20	0.20±0.04	0.11±0.02	$(5.6\pm1.1)10^{-2}$	$(3.0\pm0.6)10^{-2}$	$(1.1\pm0.3)10^{-2}$	$(2.7\pm0.8)10^{-3}$	$(6.6\pm2.3)10^{-4}$
21	0.19±0.04	0.12±0.02	$(5.6\pm1.1)10^{-2}$	$(2.9\pm0.6)10^{-2}$	$(1.1\pm0.3)10^{-2}$	$(2.7\pm0.8)10^{-3}$	$(4.7\pm1.7)10^{-4}$
22	0.19±0.04	0.13±0.03	$(6.0\pm1.2)10^{-2}$	$(2.8\pm0.6)10^{-2}$	$(1.1\pm0.3)10^{-2}$	$(2.9\pm0.9)10^{-3}$	$(6.9\pm2.4)10^{-4}$
23	0.19±0.04	0.12±0.02	$(5.9\pm1.2)10^{-2}$	$(2.6\pm0.5)10^{-2}$	$(1.0\pm0.3)10^{-2}$	$(2.6\pm0.8)10^{-3}$	$(7.6\pm2.7)10^{-4}$
24	0.19±0.04	0.13±0.03	$(5.9\pm1.2)10^{-2}$	$(2.6\pm0.5)10^{-2}$	$(1.1\pm0.3)10^{-2}$	$(2.5\pm0.8)10^{-3}$	$(8.2\pm2.9)10^{-4}$

$^{78}Kr+^{12}C \rightarrow {}^{90}Mo$			$^{82}Kr+^{12}C \rightarrow {}^{94}Mo$			$^{86}Kr+^{12}C \rightarrow {}^{98}Mo$		
E_{beam} (MeV/A)	ℓ_{max} ($\hbar$) (Bass)	ℓ_{max} ($\hbar$) (Fits)	E_{beam} (MeV/A)	ℓ_{max} ($\hbar$) (Bass)	ℓ_{max} ($\hbar$) (Fits)	E_{beam} (MeV/A)	ℓ_{max} ($\hbar$) (Bass)	ℓ_{max} ($\hbar$) (Fits)
						12.94	49.7	51
			12.19	48.3	49	11.98	49.7	50
11.37	46.8	47	11.21	48.3	48	11.06	49.7	49
10.38	46.8	46	10.27	48.3	47	10.17	49.4	48
			9.37	46.3	46	9.31	47.2	47
8.52	42.9	43	8.51	43.9	44	8.49	44.9	45
7.64	40.4	41	7.69	41.6	42	7.71	42.7	43
			6.90	39.2	39			
6.03	35.5	35	6.16	36.9	37			

	^{90}Mo		^{94}Mo		^{98}Mo	
Z	B_Z (MeV)	a_Z/a_n	B_Z (MeV)	a_Z/a_n	B_Z (MeV)	a_Z/a_n
5	30.03±0.55	1.010±0.012	30.69±0.41	1.028±0.008	30.80±0.70	1.029±0.012
6	28.50±0.72	0.990±0.016	29.72±0.54	1.004±0.011	30.60±0.71	1.007±0.012
7	32.34±0.53	0.993±0.012	33.65±0.37	1.010±0.008	34.85±0.72	1.020±0.013
8	32.22±0.51	0.972±0.011	34.84±0.38	1.010±0.008	35.77±0.71	1.004±0.012
9	35.65±0.48	0.980±0.011	38.54±0.40	1.027±0.008	38.34±0.71	1.007±0.013
10	36.07±0.48	0.989±0.011	38.50±0.33	1.019±0.008	39.66±0.57	1.032±0.010
11	36.72±0.50	0.980±0.011	40.23±0.43	1.030±0.009	40.83±0.55	1.021±0.009
12	36.63±0.51	0.976±0.011	39.84±0.36	1.013±0.007	41.76±0.52	1.017±0.009
13	37.73±0.50	0.979±0.011	41.01±0.36	1.017±0.008	42.00±0.53	1.004±0.009
14	37.59±0.48	0.972±0.011	40.87±0.38	1.004±0.008	42.71±0.46	1.003±0.008
15	38.58±0.51	0.971±0.011	41.75±0.37	1.004±0.008	42.82±0.48	0.987±0.008
16	38.95±0.56	0.972±0.013	42.11±0.47	1.003±0.010	43.21±0.47	0.986±0.008
17	40.12±0.61	0.981±0.013	42.94±0.46	1.009±0.010	44.02±0.47	0.994±0.008
18	40.96±0.64	0.994±0.014	43.17±0.52	1.009±0.011	44.46±0.45	0.996±0.008
19	41.84±0.66	1.010±0.014	43.60±0.52	1.014±0.011	44.18±0.49	0.987±0.008
20	41.33±0.68	1.001±0.015	43.83±0.54	1.018±0.011	44.46±0.47	0.992±0.008
21	41.14±0.68	0.997±0.015	44.28±0.55	1.027±0.011	44.80±0.44	0.997±0.008
22	41.39±0.74	1.005±0.016	44.54±0.58	1.035±0.012	44.35±0.47	0.991±0.008
23	40.72±0.70	0.993±0.015	44.00±0.59	1.022±0.012	44.45±0.48	0.992±0.008
24	40.46±0.66	0.990±0.014	43.23±0.59	1.008±0.014	44.32±0.48	0.992±0.008
25	39.01±0.72	0.966±0.015	42.62±0.61	0.999±0.012		

	$a_n = A/8$ (MeV)$^{-1}$			$a_n = A/9$ (MeV)$^{-1}$			$a_n = A/10$ (MeV)$^{-1}$		
Z	B_Z (MeV)	a_Z/a_n	χ^2	B_Z (MeV)	a_Z/a_n	χ^2	B_Z (MeV)	a_Z/a_n	χ^2
5	30.69±0.41	1.028±0.008	1.97	31.60±0.43	1.038±0.009	2.17	32.46±0.45	1.048±0.009	2.39
6	29.72±0.54	1.004±0.011	1.12	30.49±0.58	1.013±0.011	1.27	31.24±0.60	1.023±0.013	1.50
7	33.65±0.37	1.010±0.008	3.36	34.67±0.39	1.022±0.008	4.22	35.62±0.40	1.034±0.008	4.97
8	34.84±0.38	1.010±0.008	5.16	35.89±0.39	1.023±0.008	5.78	36.87±0.39	1.035±0.008	6.34
9	38.54±0.40	1.027±0.008	4.74	39.69±0.40	1.040±0.009	5.29	40.74±0.41	1.052±0.009	5.68
10	38.50±0.33	1.019±0.008	6.97	39.65±0.33	1.033±0.007	7.92	40.70±0.34	1.045±0.007	8.60
11	40.23±0.43	1.030±0.009	4.47	41.41±0.43	1.044±0.009	4.81	42.46±0.44	1.056±0.010	5.04
12	39.84±0.36	1.013±0.007	3.62	40.98±0.36	1.027±0.008	3.97	42.03±0.37	1.039±0.008	4.27
13	41.01±0.36	1.017±0.008	1.85	42.18±0.37	1.031±0.008	2.00	43.23±0.37	1.043±0.008	2.17
14	40.87±0.38	1.004±0.008	1.25	42.01±0.38	1.017±0.008	1.30	43.07±0.38	1.028±0.008	1.45
15	41.75±0.37	1.004±0.008	2.19	42.92±0.37	1.017±0.008	2.59	44.00±0.37	1.028±0.008	2.97
16	42.11±0.47	1.003±0.010	0.66	43.29±0.47	1.016±0.010	0.73	44.37±0.47	1.028±0.010	0.84
17	42.94±0.46	1.009±0.010	0.70	44.13±0.47	1.021±0.010	0.90	45.22±0.47	1.033±0.010	1.09
18	43.17±0.52	1.009±0.011	0.76	44.34±0.52	1.021±0.011	0.71	45.42±0.52	1.032±0.011	0.71
19	43.60±0.52	1.014±0.011	0.61	44.79±0.52	1.026±0.011	0.58	45.87±0.52	1.038±0.011	0.61
20	43.83±0.54	1.018±0.011	0.94	45.01±0.54	1.030±0.011	0.91	46.08±0.54	1.042±0.012	0.94
21	44.28±0.55	1.027±0.011	1.16	45.45±0.55	1.040±0.012	1.17	46.53±0.55	1.052±0.012	1.21
22	44.54±0.58	1.035±0.012	1.19	45.74±0.59	1.048±0.012	1.33	46.83±0.59	1.060±0.012	1.44
23	44.00±0.59	1.022±0.012	0.64	45.21±0.59	1.035±0.012	0.87	46.30±0.60	1.047±0.012	1.06
24	43.23±0.59	1.008±0.014	1.46	44.41±0.60	1.020±0.012	1.83	45.51±0.61	1.032±0.012	2.13
25	42.62±0.61	0.999±0.012	0.48	43.76±0.62	1.010±0.012	0.67	44.82±0.63	1.021±0.013	0.87

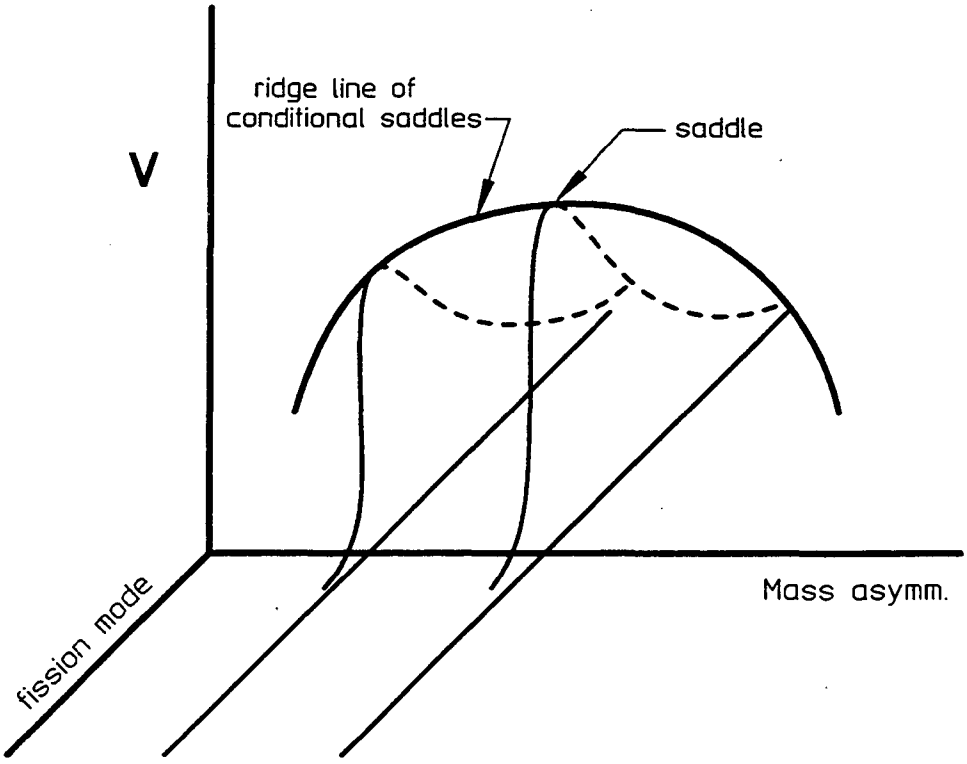
ridge line of
conditional saddles
saddle
V
Mass asymm.
fission mode

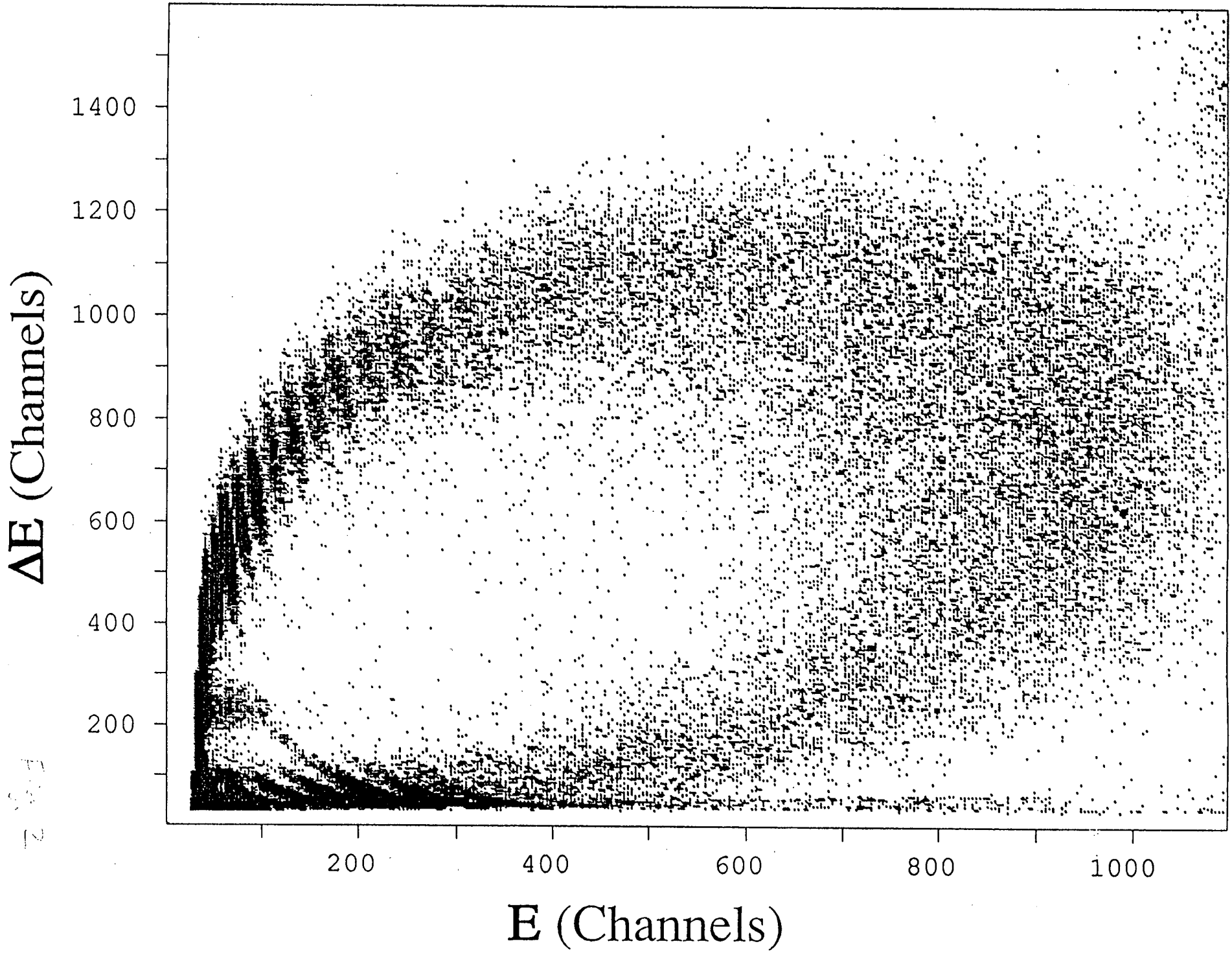
ΔE (Channels)
1400
1200
1000
800
600
400
200
200
400
600
800
1000
E (Channels)

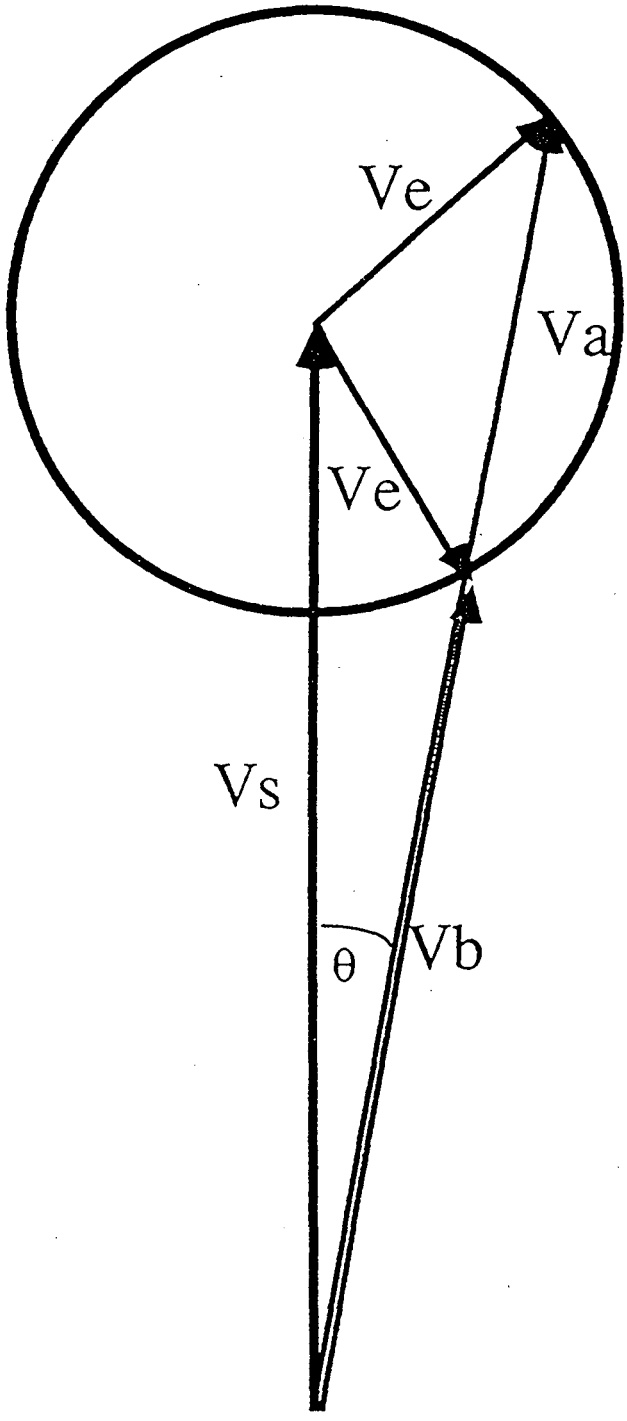

XBL 914-805

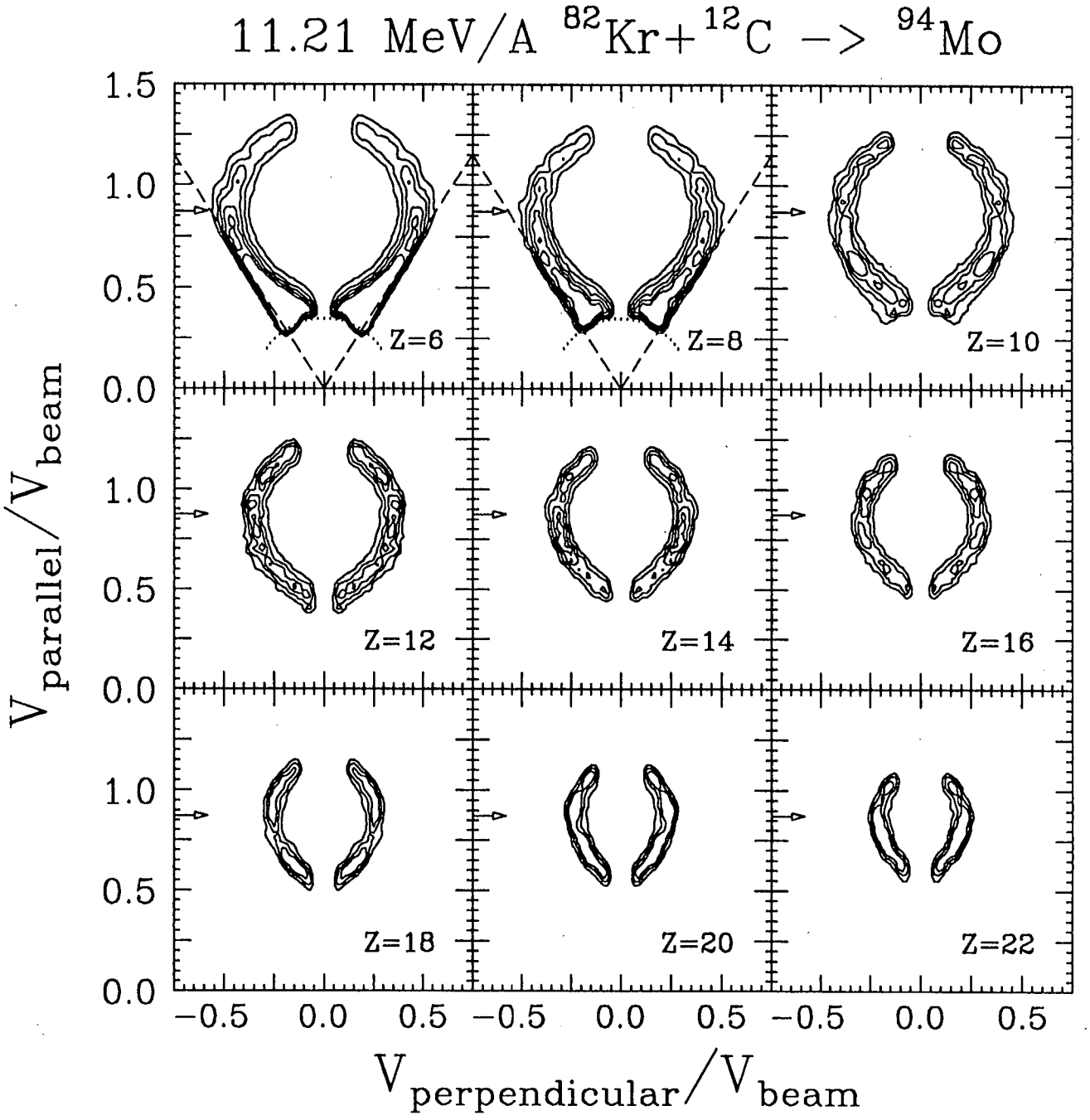
11.21 MeV/A ^{82}Kr+^{12}C -> ^{94}Mo
Z=6
Z=8
Z=10
Z=12
Z=14
Z=16
Z=18
Z=20
Z=22
1.5
1.0
0.5
0.0
−0.5
0.0
0.5
$V_{parallel}/V_{beam}$
$V_{perpendicular}/V_{beam}$

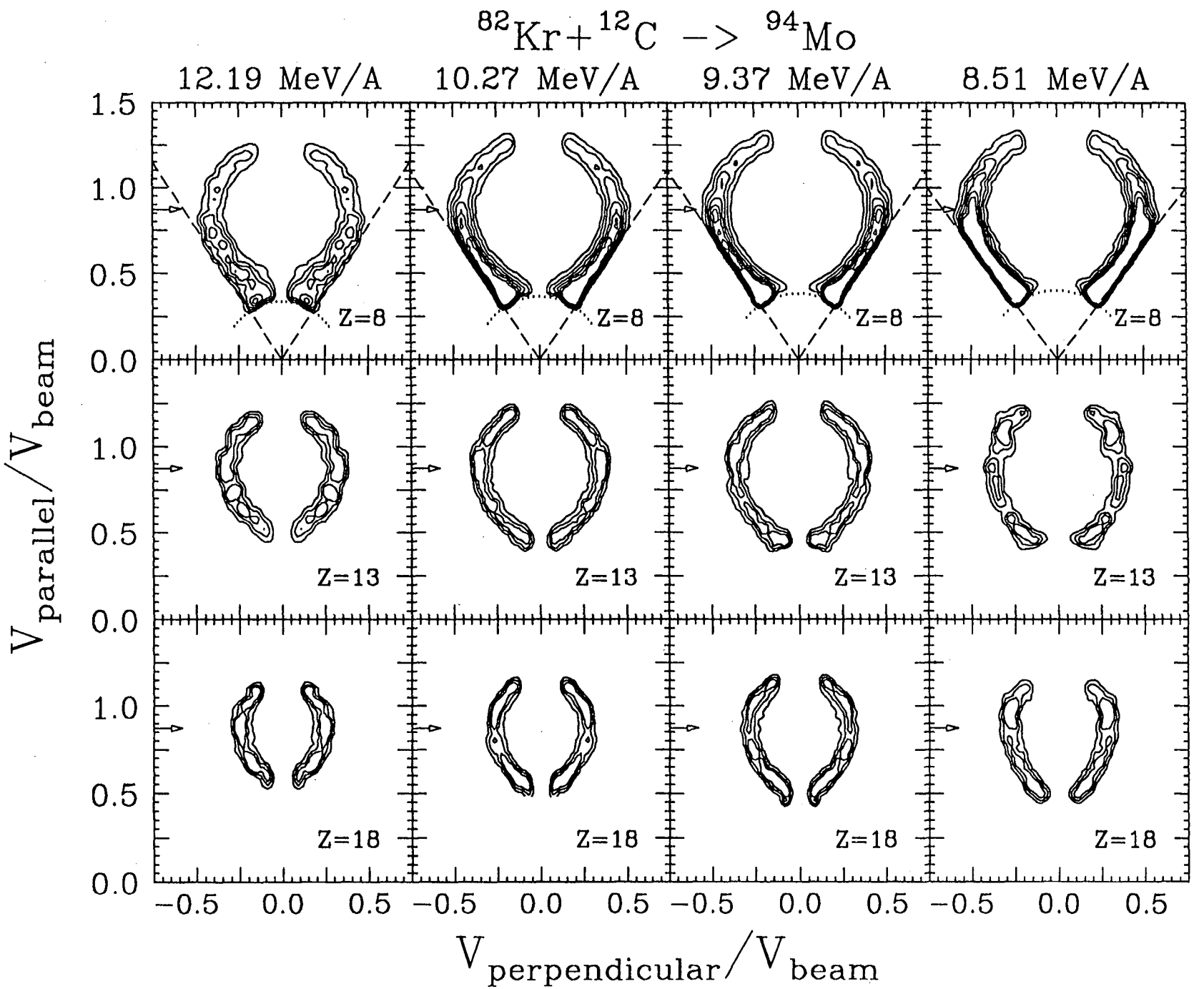
$^{82}Kr + ^{12}C \rightarrow ^{94}Mo$
12.19 MeV/A
10.27 MeV/A
9.37 MeV/A
8.51 MeV/A
Z=8
Z=13
Z=18
$V_{parallel}/V_{beam}$
$V_{perpendicular}/V_{beam}$
1.5
1.0
0.5
0.0
−0.5
0.0
0.5

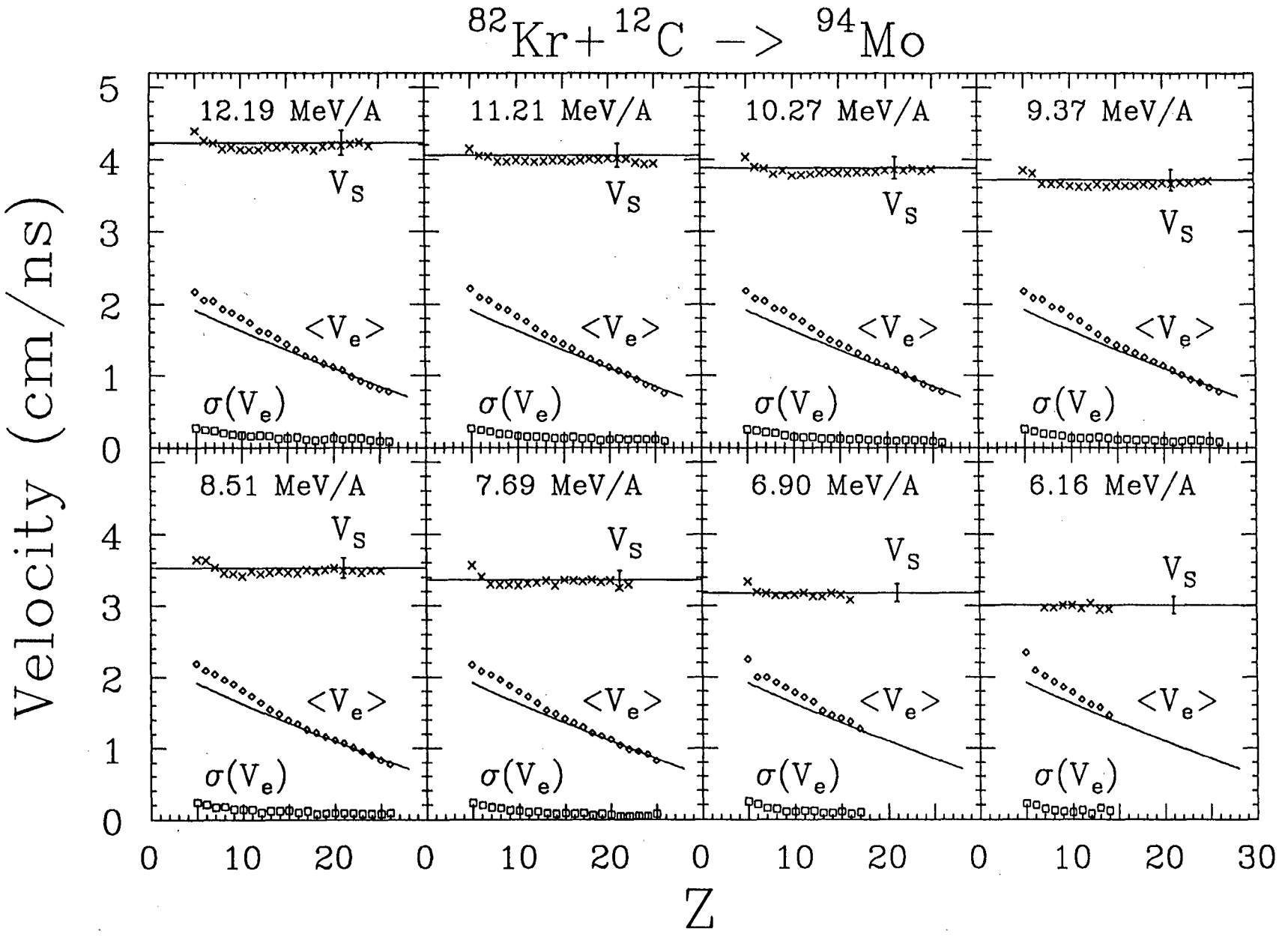
$^{82}Kr + ^{12}C \rightarrow ^{94}Mo$
12.19 MeV/A
11.21 MeV/A
10.27 MeV/A
9.37 MeV/A
8.51 MeV/A
7.69 MeV/A
6.90 MeV/A
6.16 MeV/A
V_s
$\langle V_e \rangle$
$\sigma(V_e)$
Velocity (cm/ns)
Z
0
1
2
3
4
5
10
20
30

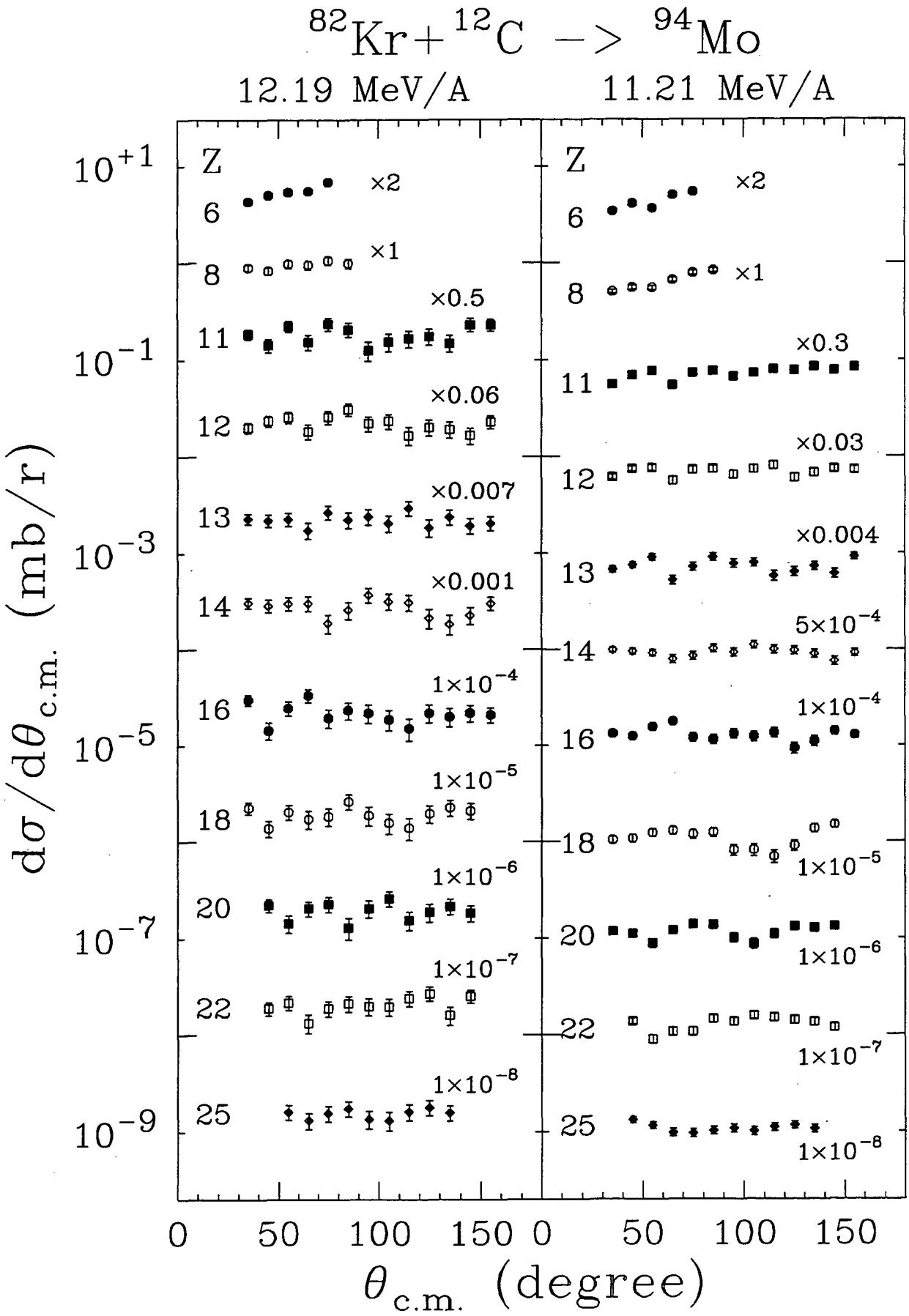
^{82}Kr+^{12}C -> ^{94}Mo
12.19 MeV/A
11.21 MeV/A
Z
6
8
11
12
13
14
16
18
20
22
25
×2
×1
×0.5
×0.06
×0.007
×0.001
1×10^{-4}
1×10^{-5}
1×10^{-6}
1×10^{-7}
1×10^{-8}
×0.3
×0.03
×0.004
5×10^{-4}
10^{+1}
10^{-1}
10^{-3}
10^{-5}
10^{-7}
10^{-9}
$d\sigma/d\theta_{c.m.}$ (mb/r)
0
50
100
150
$\theta_{c.m.}$ (degree)

Fig 2

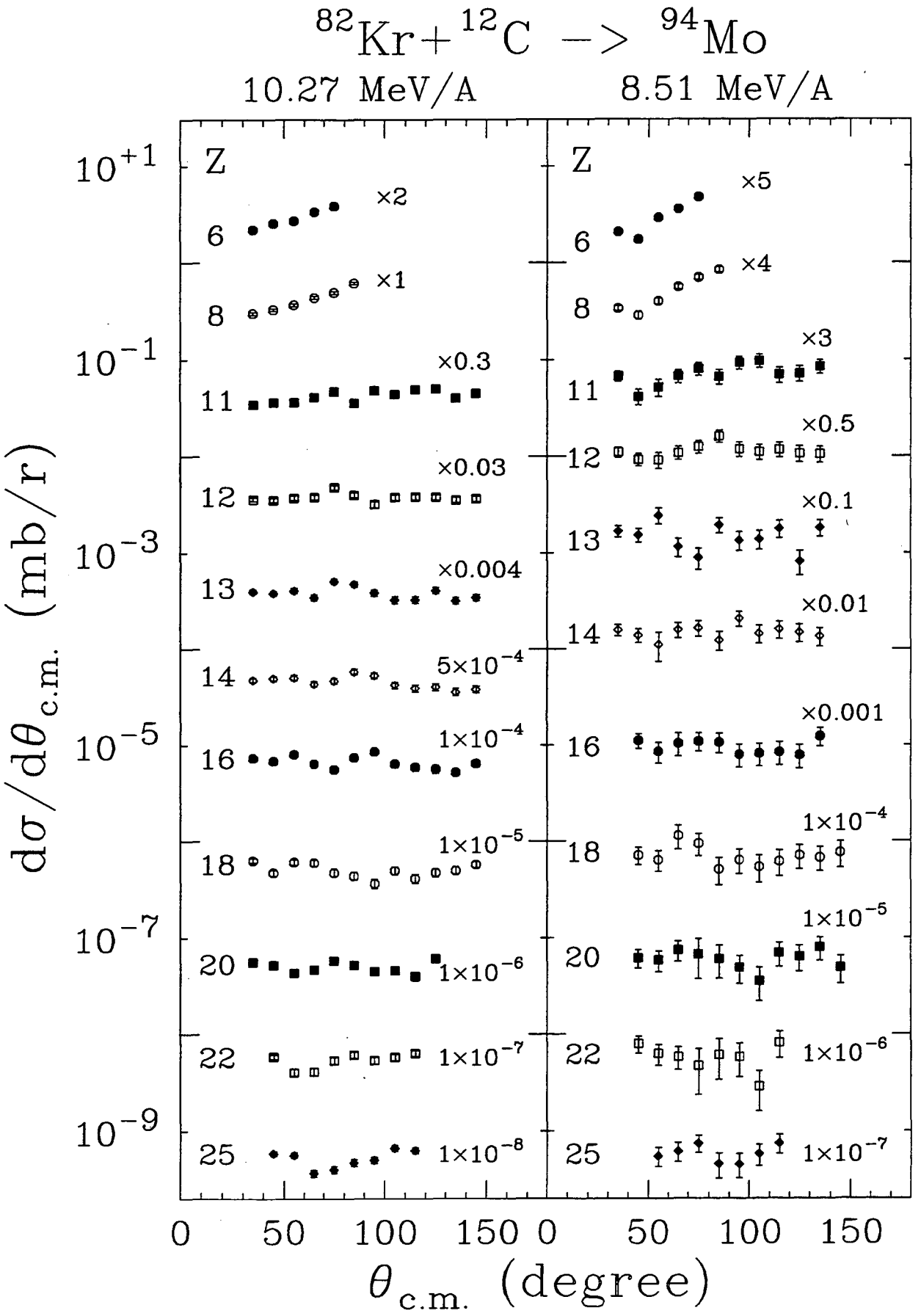
^{82}Kr+^{12}C -> ^{94}Mo
10.27 MeV/A
8.51 MeV/A
Z
6
8
11
12
13
14
16
18
20
22
25
×2
×1
×0.3
×0.03
×0.004
5×10^{-4}
1×10^{-4}
1×10^{-5}
1×10^{-6}
1×10^{-7}
1×10^{-8}
×5
×4
×3
×0.5
×0.1
×0.01
×0.001
1×10^{-4}
1×10^{-5}
1×10^{-6}
1×10^{-7}
10^{+1}
10^{-1}
10^{-3}
10^{-5}
10^{-7}
10^{-9}
dσ/dθ$_{c.m.}$ (mb/r)
0
50
100
150
θ$_{c.m.}$ (degree)

Fig. 6

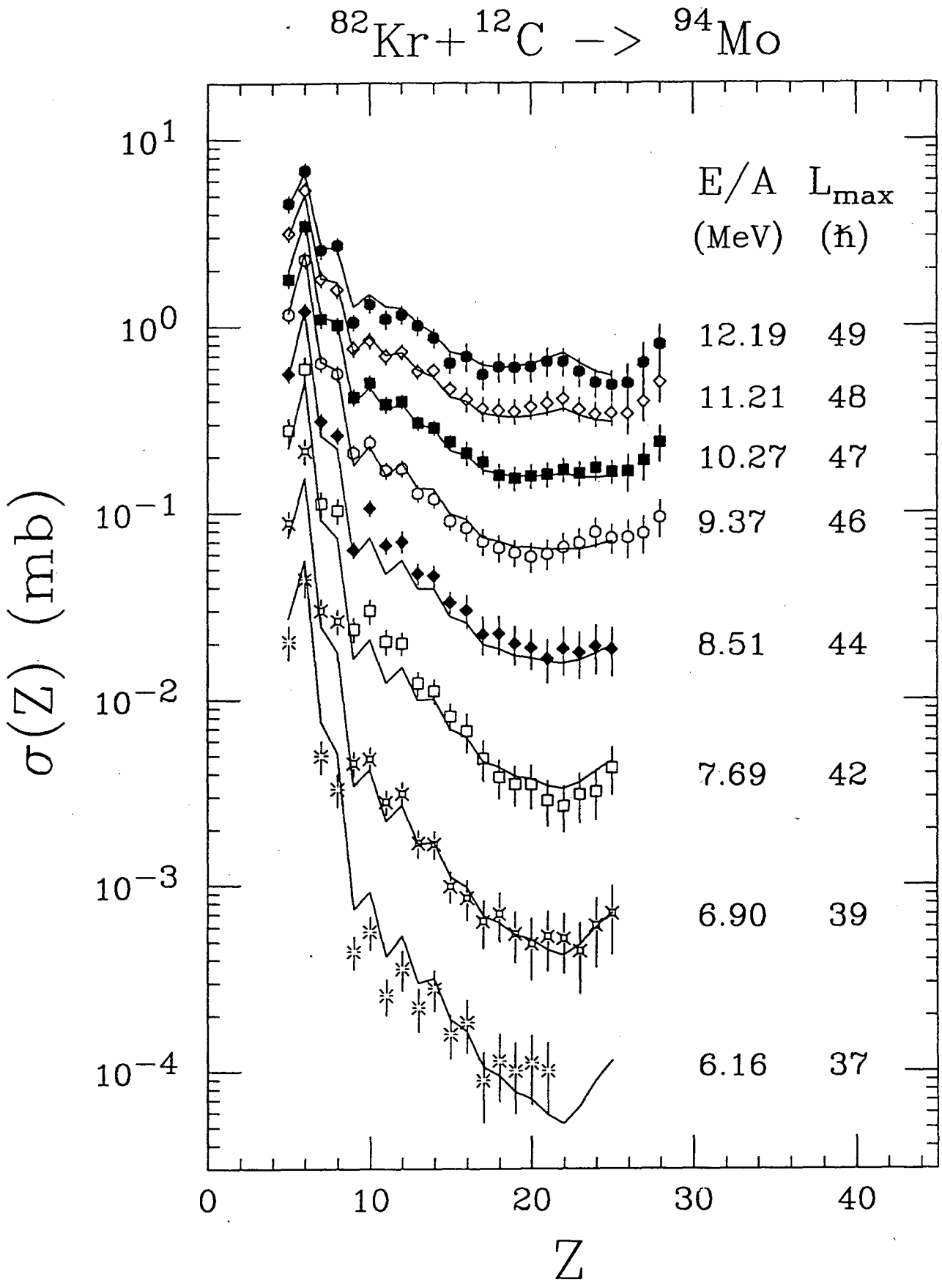
$^{82}Kr + ^{12}C \rightarrow ^{94}Mo$
E/A (MeV)
L_{max} (ħ)
12.19 49
11.21 48
10.27 47
9.37 46
8.51 44
7.69 42
6.90 39
6.16 37
$\sigma(Z)$ (mb)
Z
10^1
10^0
10^{-1}
10^{-2}
10^{-3}
10^{-4}
0
10
20
30
40

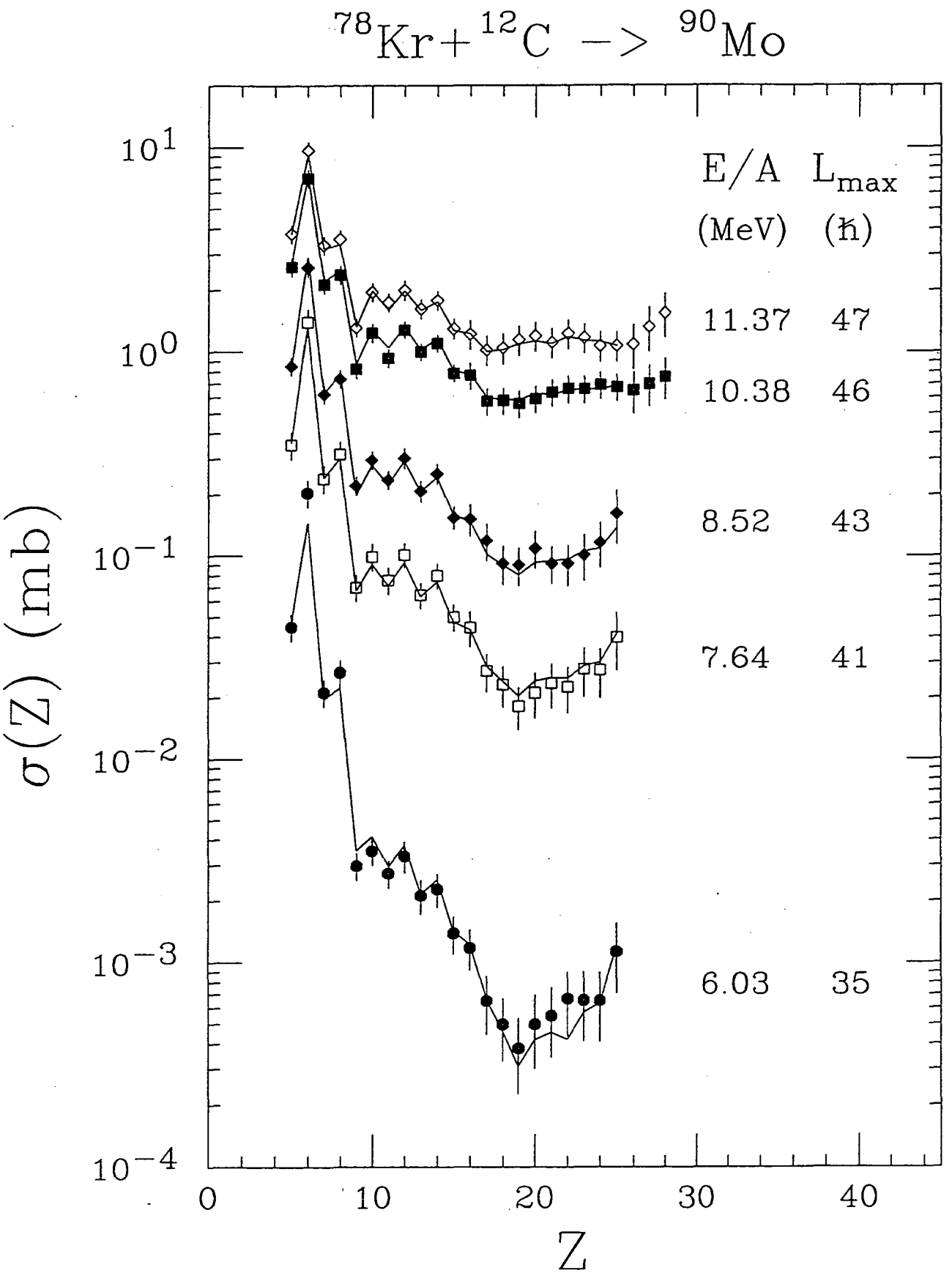
$^{78}Kr + ^{12}C \rightarrow ^{90}Mo$
E/A (MeV)
L_{max} (ħ)
11.37 47
10.38 46
8.52 43
7.64 41
6.03 35
$\sigma(Z)$ (mb)
Z
10^1
10^0
10^{-1}
10^{-2}
10^{-3}
10^{-4}
0
10
20
30
40

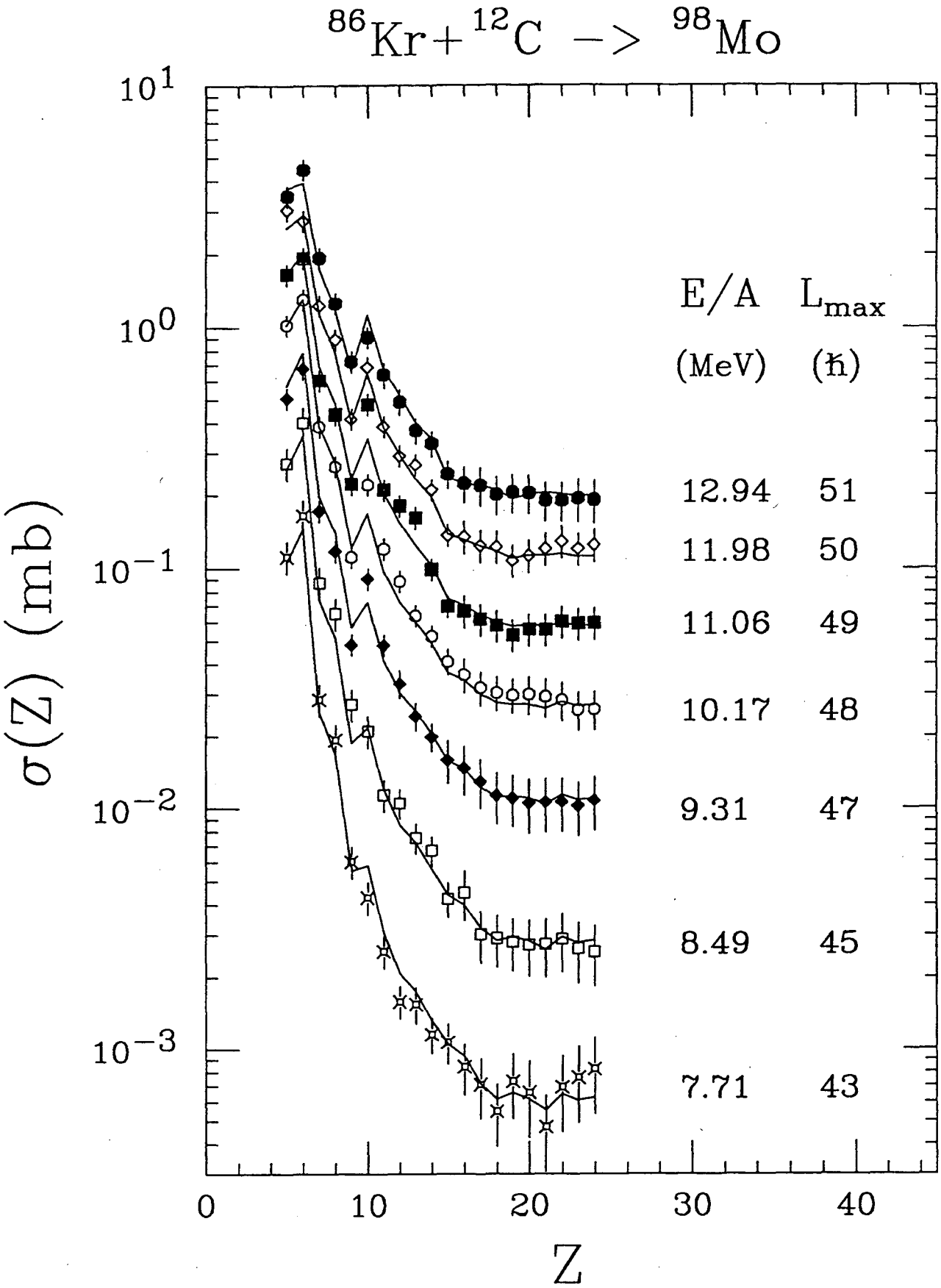
$^{86}Kr + ^{12}C \rightarrow ^{98}Mo$
10^1
10^0
10^{-1}
10^{-2}
10^{-3}
$\sigma(Z)$ (mb)
E/A (MeV)
L_{max} ($\hbar$)
12.94 51
11.98 50
11.06 49
10.17 48
9.31 47
8.49 45
7.71 43
0
10
20
30
40
Z

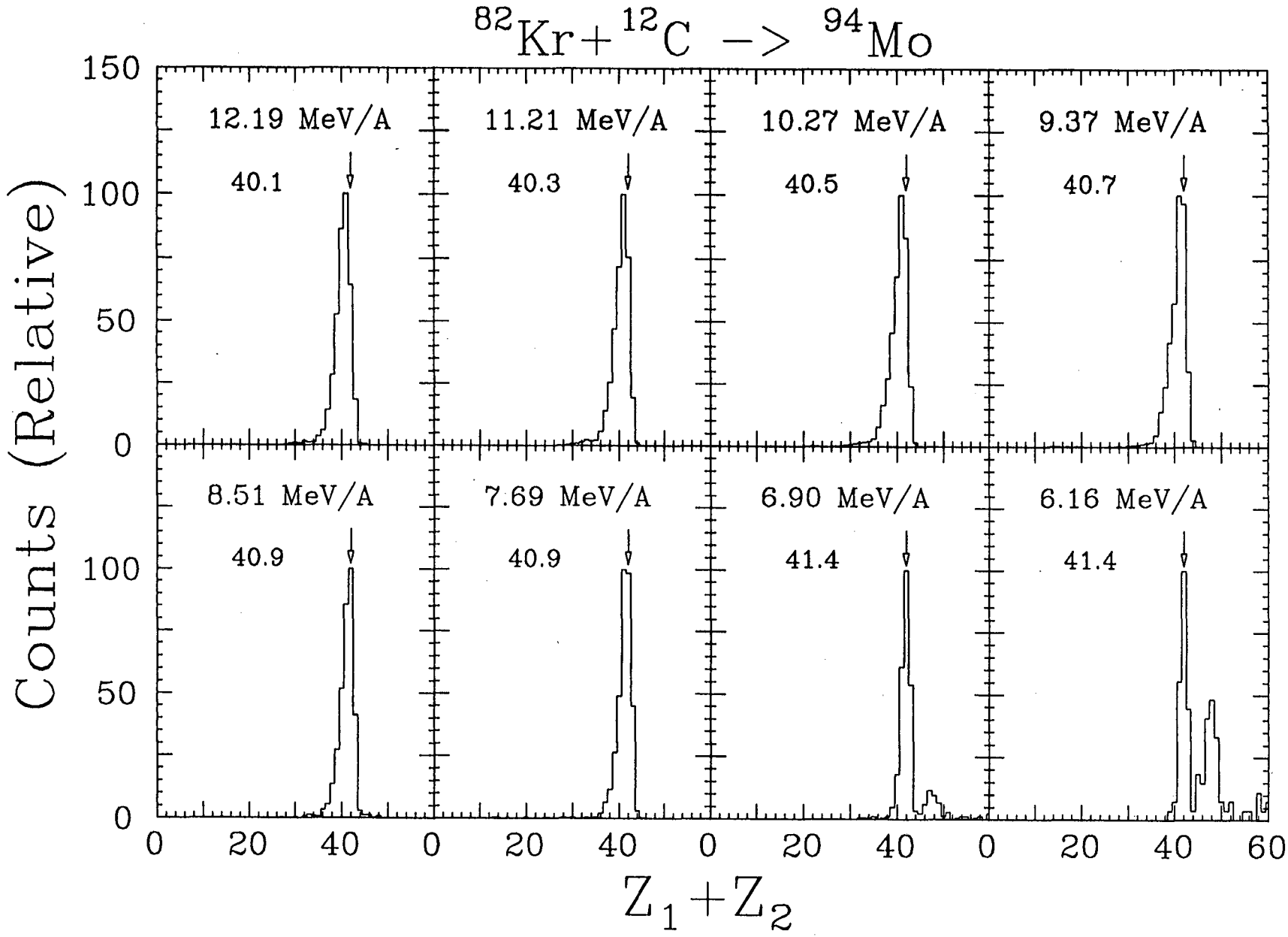
$^{82}Kr + ^{12}C \rightarrow ^{94}Mo$
12.19 MeV/A
40.1
11.21 MeV/A
40.3
10.27 MeV/A
40.5
9.37 MeV/A
40.7
8.51 MeV/A
40.9
7.69 MeV/A
40.9
6.90 MeV/A
41.4
6.16 MeV/A
41.4
Counts (Relative)
$Z_1 + Z_2$
0
50
100
150
0
20
40
60

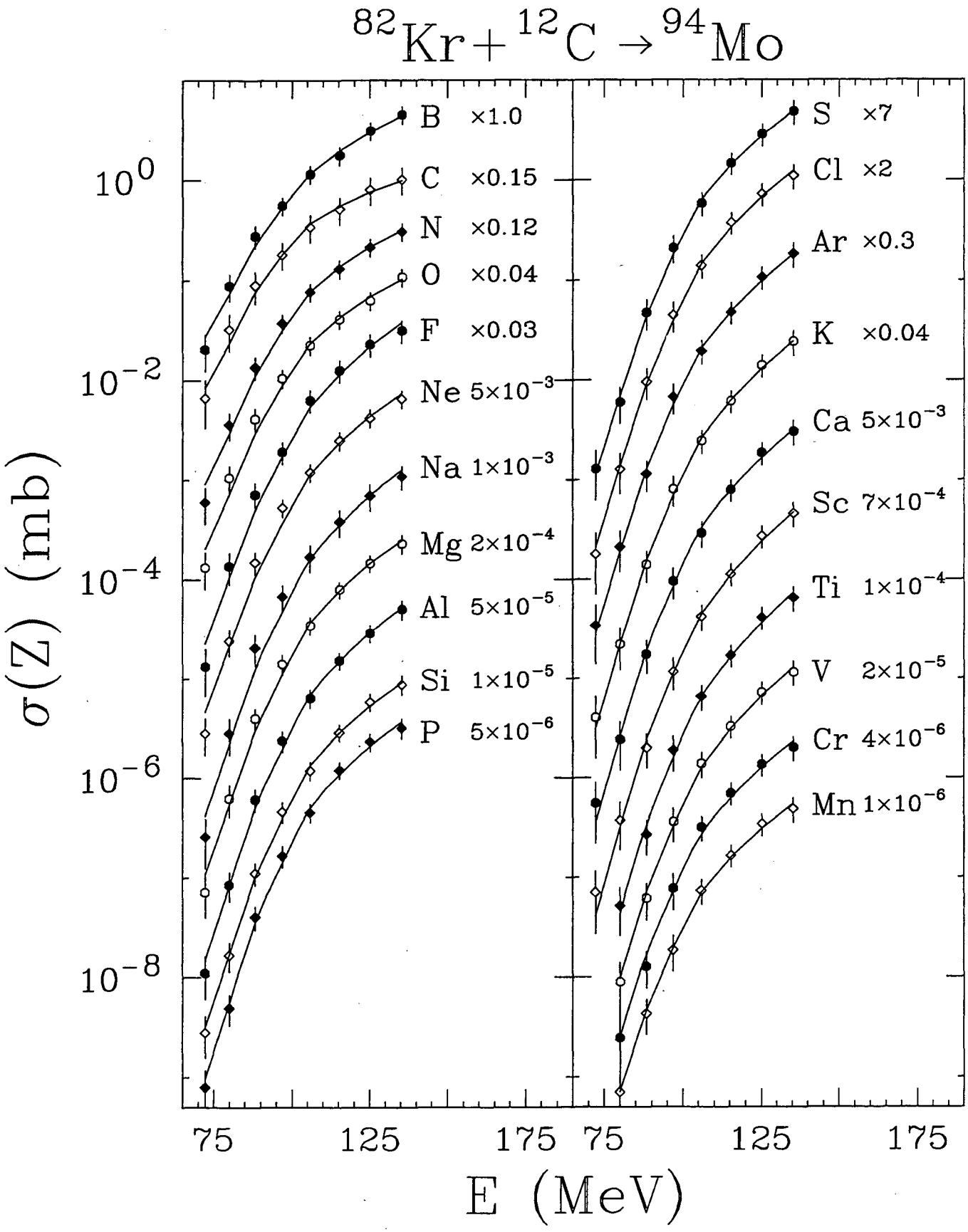
$^{82}Kr + ^{12}C \rightarrow ^{94}Mo$
B ×1.0
C ×0.15
N ×0.12
O ×0.04
F ×0.03
Ne 5×10^{-3}
Na 1×10^{-3}
Mg 2×10^{-4}
Al 5×10^{-5}
Si 1×10^{-5}
P 5×10^{-6}
S ×7
Cl ×2
Ar ×0.3
K ×0.04
Ca 5×10^{-3}
Sc 7×10^{-4}
Ti 1×10^{-4}
V 2×10^{-5}
Cr 4×10^{-6}
Mn 1×10^{-6}
10^{0}
10^{-2}
10^{-4}
10^{-6}
10^{-8}
σ(Z) (mb)
75
125
175
E (MeV)

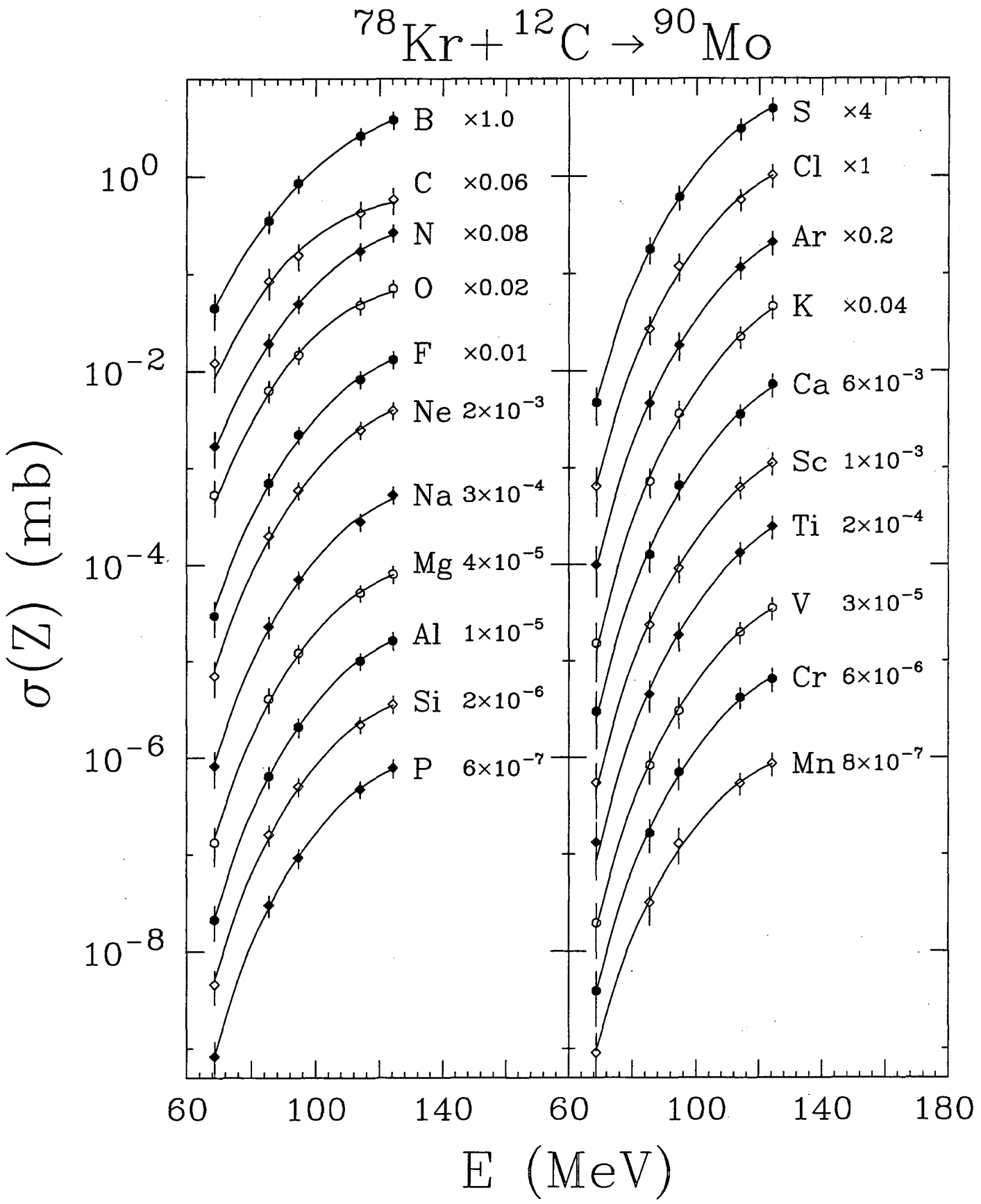
$^{78}Kr + ^{12}C \rightarrow ^{90}Mo$
B ×1.0
C ×0.06
N ×0.08
O ×0.02
F ×0.01
Ne 2×10^{-3}
Na 3×10^{-4}
Mg 4×10^{-5}
Al 1×10^{-5}
Si 2×10^{-6}
P 6×10^{-7}
S ×4
Cl ×1
Ar ×0.2
K ×0.04
Ca 6×10^{-3}
Sc 1×10^{-3}
Ti 2×10^{-4}
V 3×10^{-5}
Cr 6×10^{-6}
Mn 8×10^{-7}
10^{0}
10^{-2}
10^{-4}
10^{-6}
10^{-8}
σ(Z) (mb)
60
100
140
60
100
140
180
E (MeV)

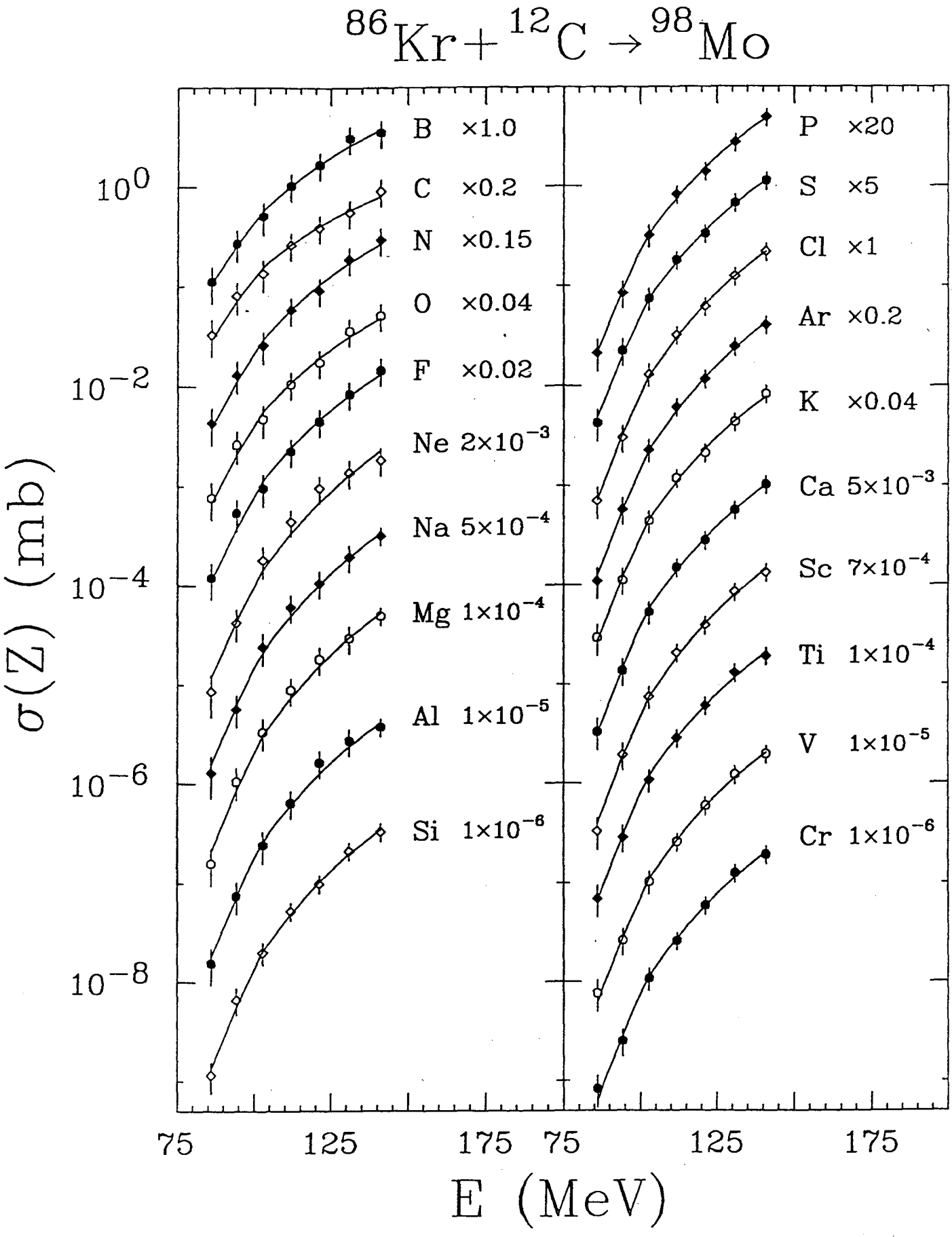
$^{86}Kr + ^{12}C \rightarrow ^{98}Mo$
B ×1.0
C ×0.2
N ×0.15
O ×0.04
F ×0.02
Ne 2×10^{-3}
Na 5×10^{-4}
Mg 1×10^{-4}
Al 1×10^{-5}
Si 1×10^{-6}
P ×20
S ×5
Cl ×1
Ar ×0.2
K ×0.04
Ca 5×10^{-3}
Sc 7×10^{-4}
Ti 1×10^{-4}
V 1×10^{-5}
Cr 1×10^{-6}
10^{0}
10^{-2}
10^{-4}
10^{-6}
10^{-8}
σ(Z) (mb)
75
125
175
75
125
175
E (MeV)

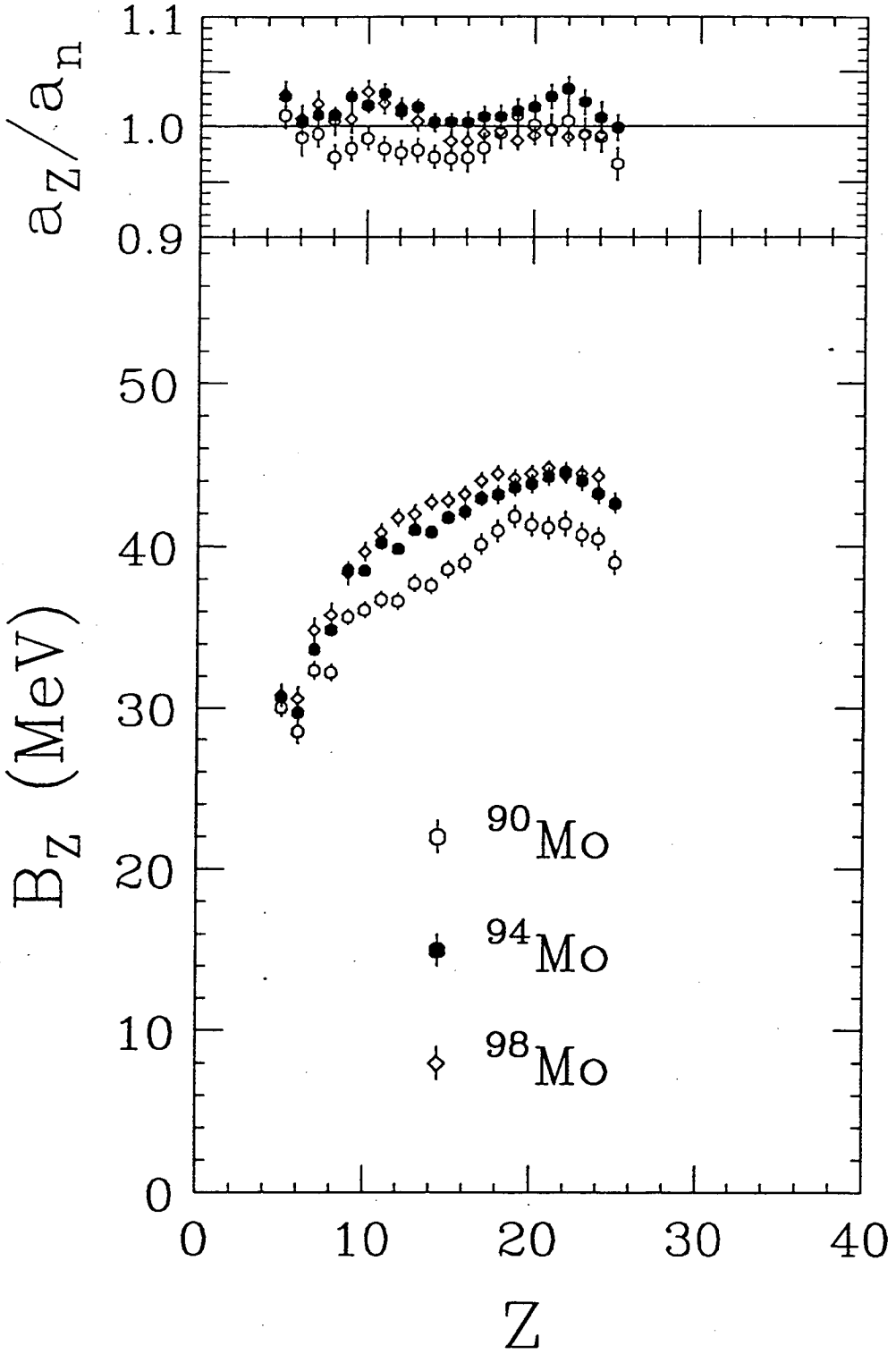
1.1
1.0
0.9
a_Z/a_n
50
40
30
20
10
0
B_Z (MeV)
^{90}Mo
^{94}Mo
^{98}Mo
0
10
20
30
40
Z

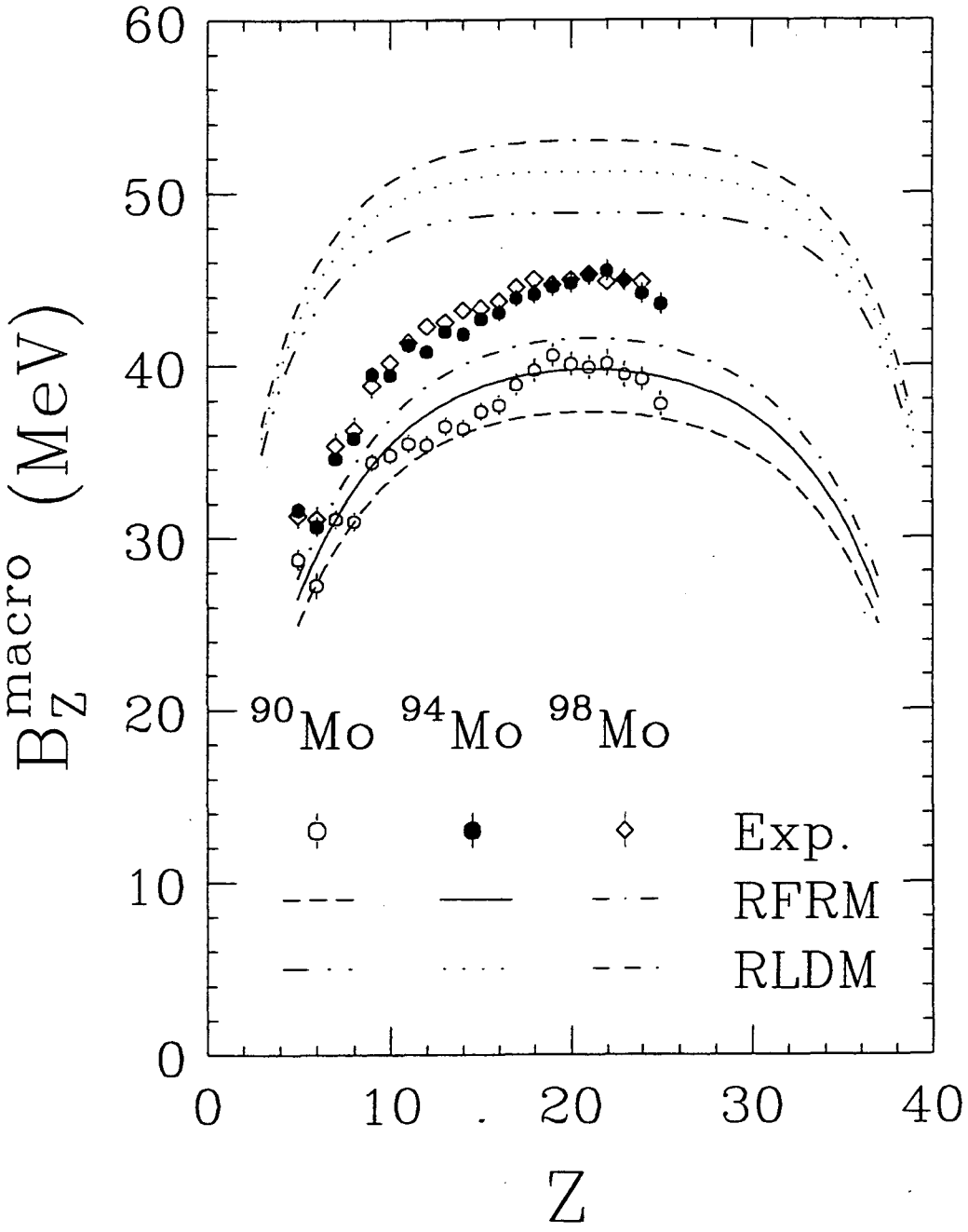
60
50
40
30
20
10
0
0
10
20
30
40
Z
B_Z^{macro} (MeV)
^{90}Mo
^{94}Mo
^{98}Mo
Exp.
RFRM
RLDM

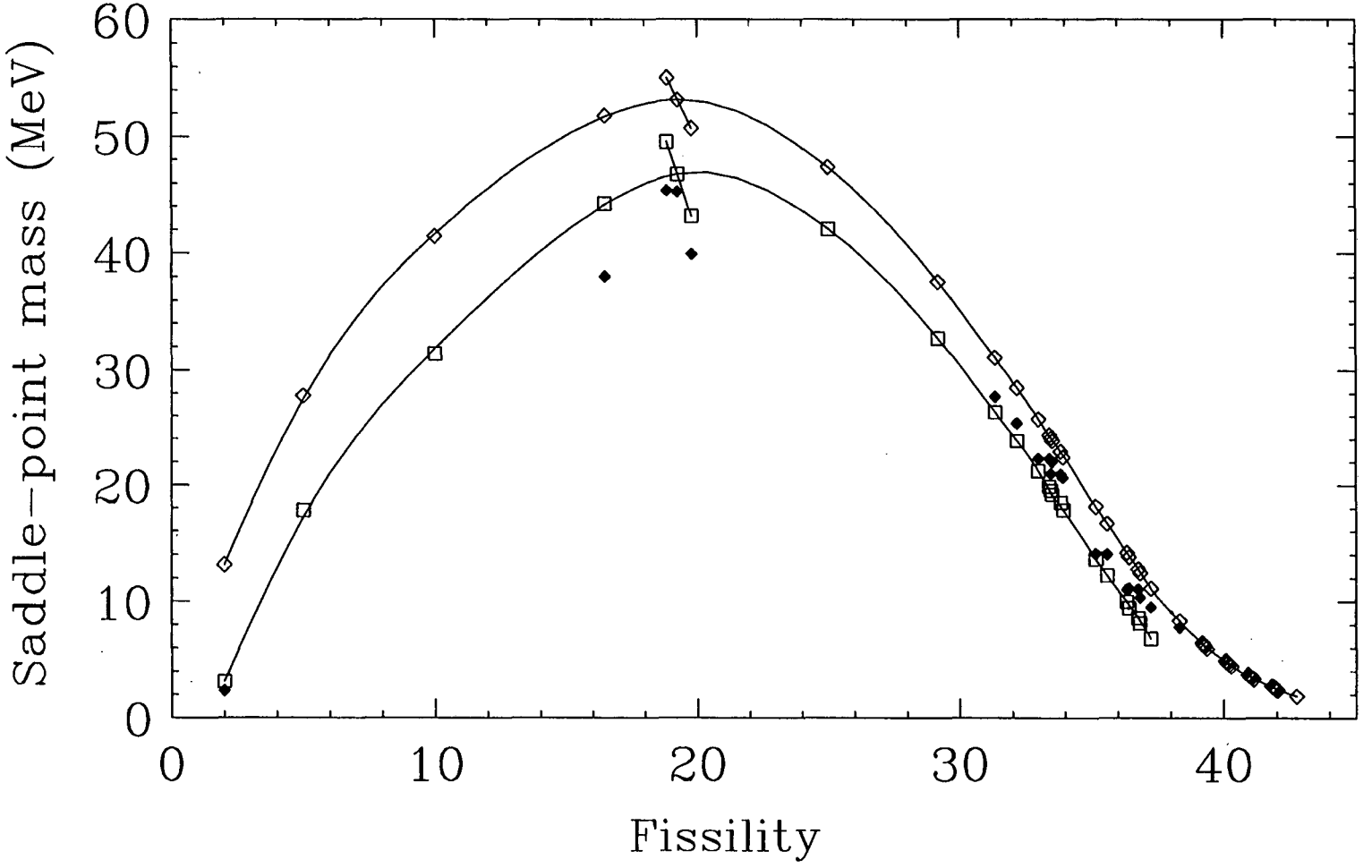
Saddle-point mass (MeV)
Fissility
0
10
20
30
40
50
60
0
10
20
30
40

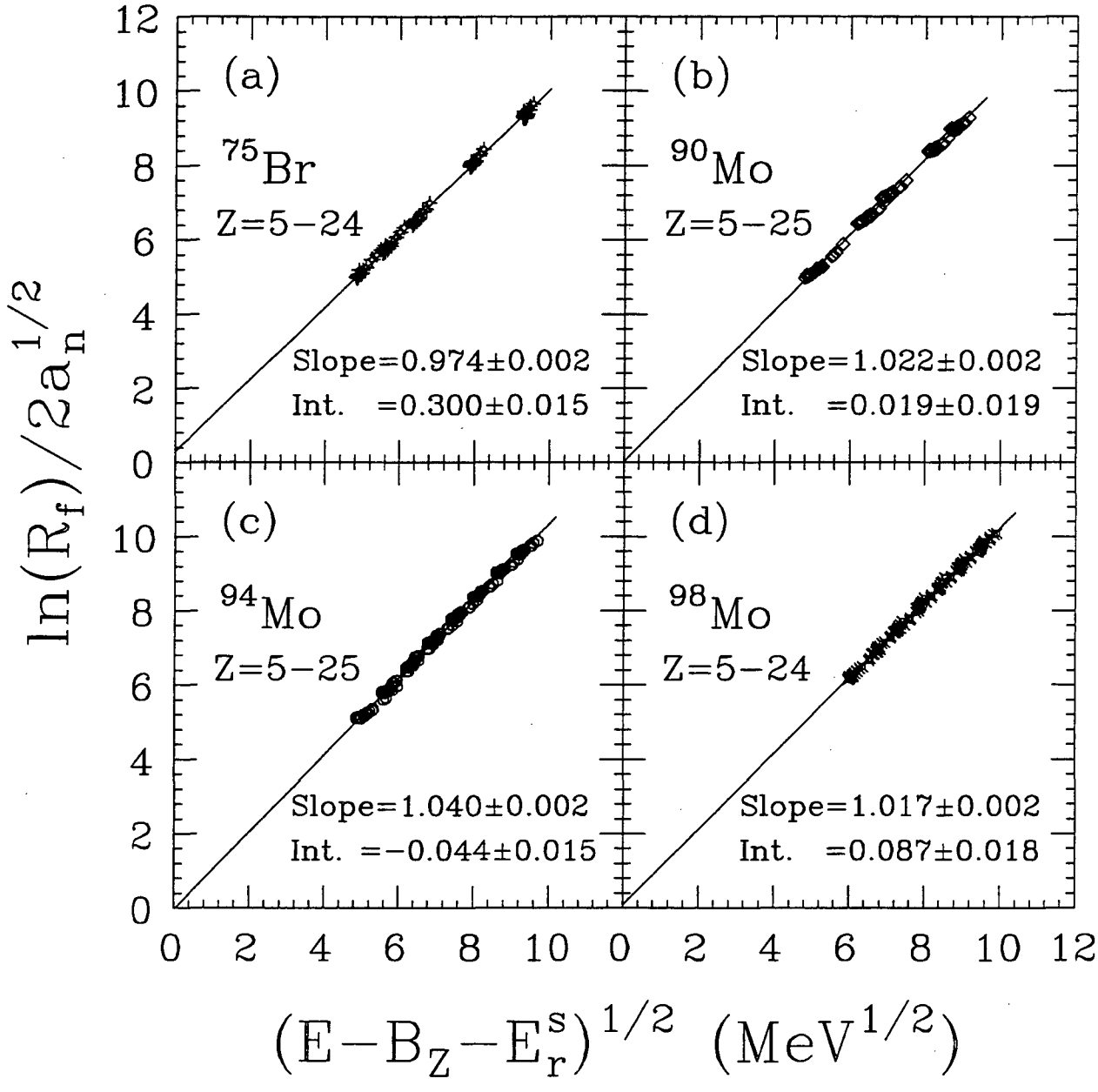
(a)
^{75}Br
Z=5−24
Slope=0.974±0.002
Int. =0.300±0.015
(b)
^{90}Mo
Z=5−25
Slope=1.022±0.002
Int. =0.019±0.019
(c)
^{94}Mo
Z=5−25
Slope=1.040±0.002
Int. =−0.044±0.015
(d)
^{98}Mo
Z=5−24
Slope=1.017±0.002
Int. =0.087±0.018
$\ln(R_f)/2a_n^{1/2}$
$(E-B_Z-E_r^s)^{1/2}$ $(MeV^{1/2})$

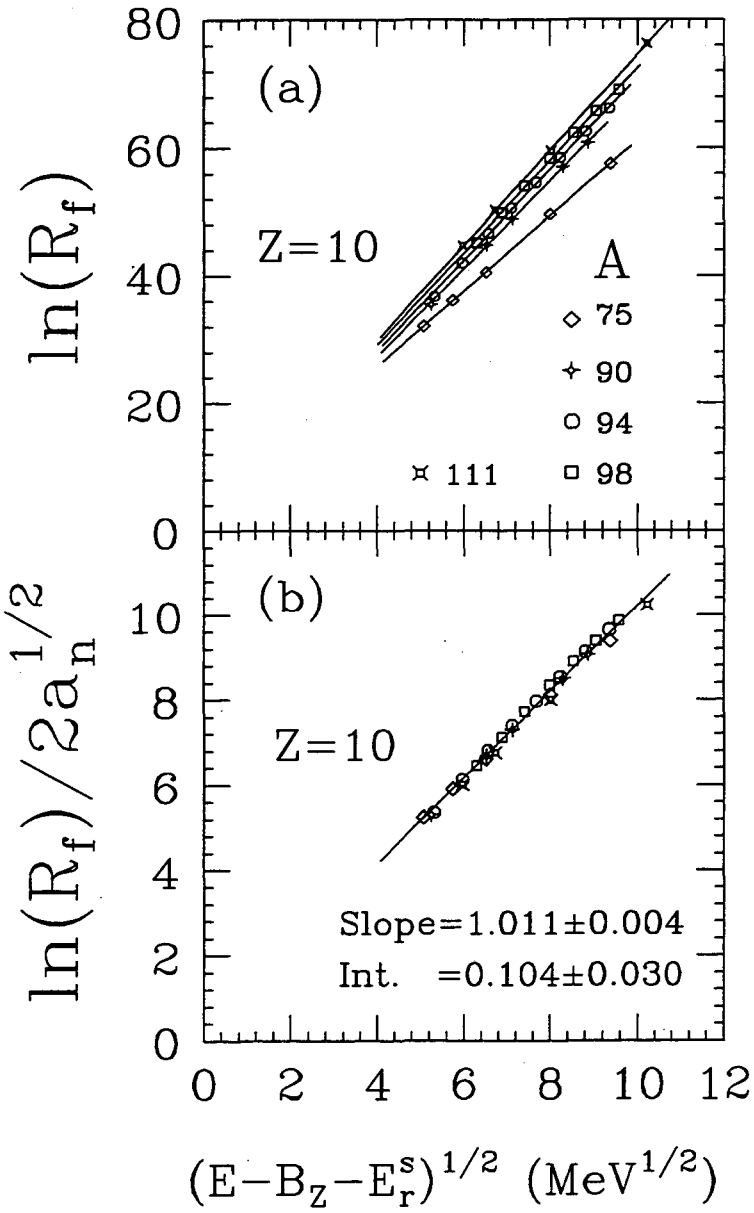
(a)
Z=10
A
75
90
94
111
98
ln(R_f)
(b)
Z=10
Slope=1.011±0.004
Int. =0.104±0.030
ln(R_f)/2a_n^{1/2}
(E−B_Z−E_r^s)^{1/2} (MeV^{1/2})

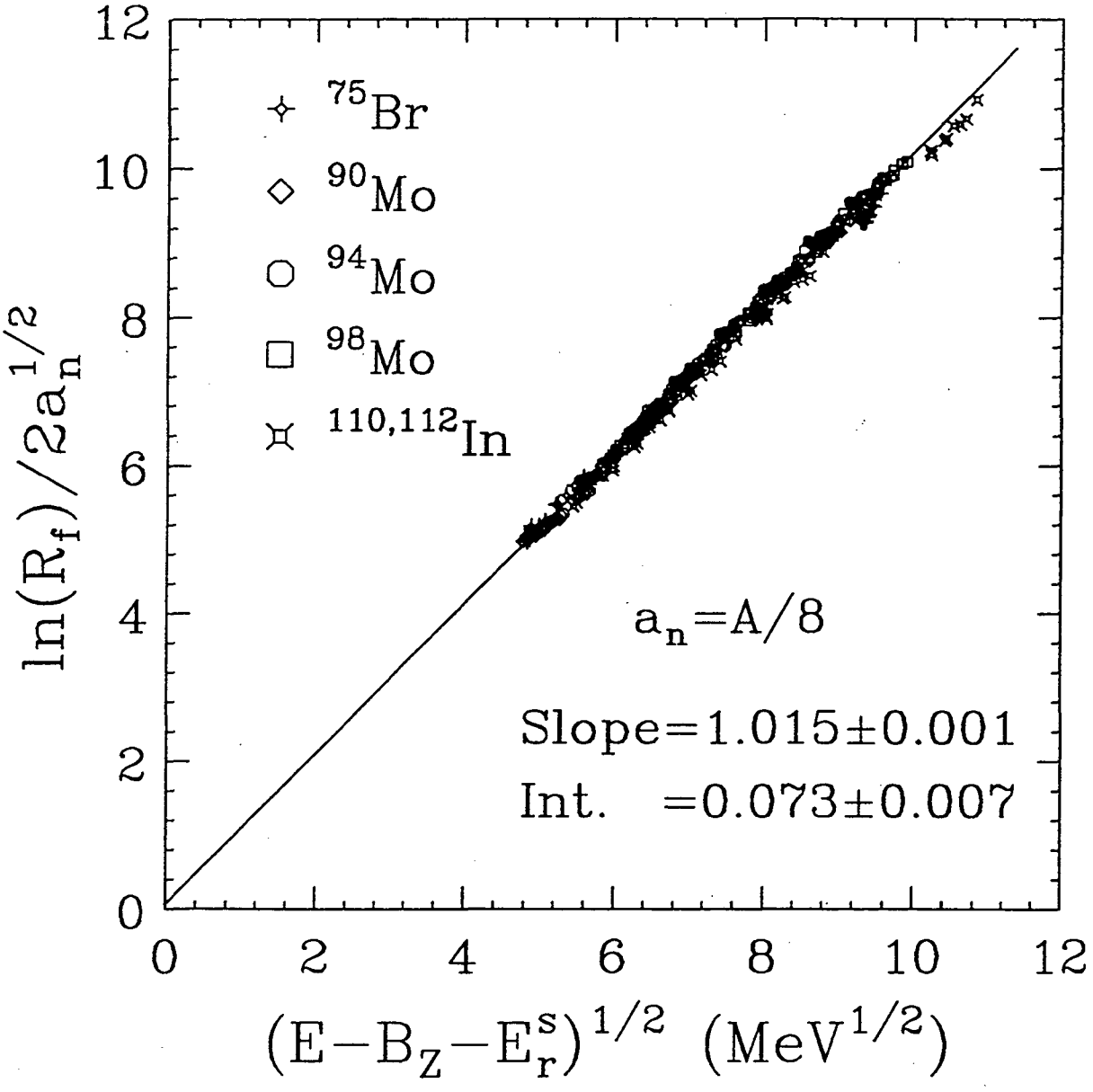
^{75}Br
^{90}Mo
^{94}Mo
^{98}Mo
^{110,112}In
a_n=A/8
Slope=1.015±0.001
Int. =0.073±0.007
$\ln(R_f)/2a_n^{1/2}$
$(E-B_Z-E_r^s)^{1/2}$ $(MeV^{1/2})$
0
2
4
6
8
10
12

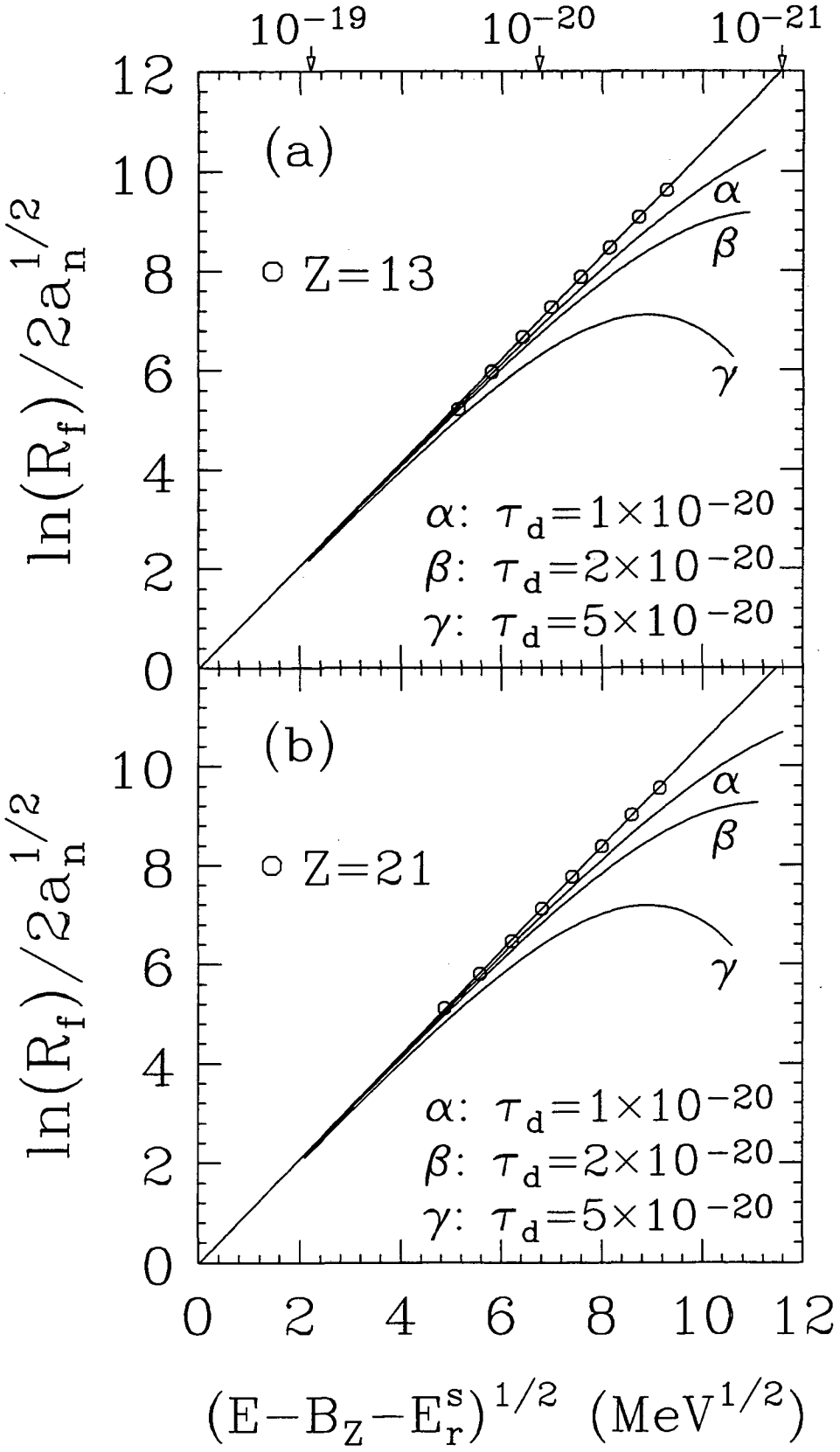
10^{-19}
10^{-20}
10^{-21}
(a)
○ Z=13
α
β
γ
α: $\tau_d=1\times10^{-20}$
β: $\tau_d=2\times10^{-20}$
γ: $\tau_d=5\times10^{-20}$
(b)
○ Z=21
α
β
γ
α: $\tau_d=1\times10^{-20}$
β: $\tau_d=2\times10^{-20}$
γ: $\tau_d=5\times10^{-20}$
$\ln(R_f)/2a_n^{1/2}$
$(E-B_Z-E_r^s)^{1/2}$ $(MeV^{1/2})$

Fig 22

Ernest Orlando Lawrence Berkeley National Laboratory
One Cyclotron Road | Berkeley, California 94720

Prepared for the U.S. Department of Energy under Contract No. DE-AC03-76SF00098

AAX971
LBL Libraries